CRF release from a unique subpopulation of accumbal neurons constrains action-outcome acquisition in reward learning

Elizabeth A. Eckenwiler[1,2], Anna E. Ingebretson[1,2], Jeffrey J. Stolley[1,2], Christopher L. Petersen[1,2], Maxine A. Fusaro[1,2], Jack M. Ross[1,2], Alyssa M. Romportl[1,2], Eera M. Kale[1,2], Michael S. Clark[3] and Julia C. Lemos[1,2]*

*Corresponding author: Dr. Julia C. Lemos
jlemos@umn.edu
321 Church Street
Minneapolis, MN 55406

Affiliations

1. Department of Neuroscience, University of Minnesota-Twin Cities, Minneapolis, MN.

2. Medical Discovery Team on Addiction, University of Minnesota, Minneapolis, MN.

3. Department of Psychiatry and Behavioral Sciences, University of Washington, Seattle, WA.

Running Title**: Accumbal CRF release constrains outcome-action acquisition**

Keywords: Corticotropin-releasing factor, nucleus accumbens, spiny projection neuron, striatum, reward learning, mesolimbic system, stress, novelty, neuropeptides, electrophysiology

Acknowledgements: This study was funded by K99/R00 Pathway to Independence award (MH109627 JCL), NIMH BRAINS R01 (MH122749 JCL), and NIDA F31 NRSA (DA059436 EAE). This work was supported by the resources and staff at the University of Minnesota University Imaging Centers (UIC, SCR_020997). We thank Dr. Veronica Alvarez for the use of equipment and reagents. We thank Mariah Blegen for assistance with qPCR. We thank Rachel Dick for some technical assistance. Dr. Kavya Devarakonda contributed key edits to the manuscript. The authors declare no competing financial interests.

Author Contributions: conceptualization: E.A.E. and J.C.L.; formal analysis: E.A.E., A.E.I., J.J.S., C.L.P., M.F., J.M.R., A.M.R., E.M.K., J.C.L.; funding acquisition: E.A.E., J.C.L.; investigation: E.A,E, A.E.I, J.J.S, C.L.P, M.F., J.M.R, A.M.R., E.M.K, J.C.L; methodology: E.A.E., A.E.I., C.L.P., J.C.L.; project administration and supervision: E.A.E., A.E.I., C.L.P., J.C.L.; resources: M.S.C., J.C.L.; software: E.A.E., A.E.I., J.C.L.; visualization: E.A.E., A.E.I., J.C.L.; writing – original draft: E.A.E., J.C.L.; writing - review & editing: E.A.E., A.E.I., J.C.L.

Summary

Neurons within the dorsal and ventral striatum are often parsed into the two classes of spiny projection neurons, D1-containing and D2-containing neurons, and several classes of interneuron based on structure and function. However, with advanced technology and the appreciation of the importance of peptidergic neuromodulation, striatal neurons can be further and even differentially classified based on peptidergic content and function. The existence of a sparse population of neurons containing corticotropin releasing factor (CRF) in the nucleus accumbens (NAc) has been known for several decades. However, for the first time, we provide a comprehensive analysis of their identity and functional role in shaping reward learning, a critical function of the NAc. Here we show that the vast majority of NAc CRF neurons are spiny projection neurons (SPNs) comprised of D1-, D2- or D1/D2-containing SPNs. This unique population of NAc CRF neurons project to ventral pallidum and ventral midbrain and display both canonical and non-canonical SPN firing properties. We demonstrate that NAc CRF neurons track reward outcomes during operant reward learning and that CRF release from these neurons acts to constrain initial acquisition of action-outcome learning.

Introduction

The nucleus accumbens (NAc) drives several evolutionarily conserved behaviors, including environmental exploration and reward learning[1,2]. It is a part of the ventral striatum that interfaces with several different glutamatergic, monoaminergic and peptidergic inputs to influence motivated behaviors[3,4]. There is a complex, albeit unresolved, relationship between the ventral and dorsal striatum on a variety of levels. Like the dorsal striatum, the NAc contains two populations of spiny projection neurons (SPNs) that can be distinguished by their peptidergic expression, intrinsic excitability, dopamine receptor expression and projection patterns[3,5]. Synchronous optogenetic stimulation of these distinct SPN populations often results in opposite behavioral responses — though this canonical behavioral pattern has recently been challenged[6-8]. Both the dorsal striatum and NAc also contain a number of interneuron subtypes, including cholinergic interneurons and a number of molecularly and functionally distinct GABAergic interneurons[3,9,10]. Behaviorally, it is thought that the dorsal striatum controls procedural learning, habit formation (dorsolateral) and goal-directed actions (dorsomedial), while the NAc supports associative learning, hedonic pleasure and motivation[11]. These differences in the behavioral function of the dorsal and ventral striatum have largely been attributed to differences in inputs[12]. However, recent studies have begun to reveal fine-tuned differences in molecular expression in the NAc compared to the dorsal striatum, which may contribute to their disparate behavioral roles[13-15].

For four decades, it has been known that there is a sparse population of neurons in the rat NAc that contain the neuropeptide neurotransmitter corticotropin-releasing factor (CRF)[16]. This initial immunohistochemical study found that these CRF neurons, although sparse, are far more abundant in the NAc compared to the dorsal striatum, suggesting that CRF release from these neurons may be particularly important for NAc-dependent behaviors. These accumbal CRF neurons have been presumed to be some type of interneuron, primarily due to their scarcity. Yet, optogenetic stimulation of this population increases cFos activity in other brain regions such as the ventral tegmental

area, ventral pallidum and bed nucleus of the stria terminalis (BNST), in addition to within the NAc, leaving open the possibility for long-range projections[17].

CRF has historically been characterized as a peptide that encodes the aversive properties of stress. However, within the mesocorticolimbic pathway it may play a more complex role, such as the invigoration of exploratory and appetitive behaviors[18-22]. In 2021, Baumgartner and colleagues demonstrated that optogenetic stimulation of CRF+ neurons in the rat NAc promoted reward consumption and supported intracranial self-stimulation by increasing incentive motivation, not by regulating aversion[17]. These results broadened the field's conception of CRF's role in the brain and was, to our knowledge, the first behavior linked to CRF neurons in the NAc. Nevertheless, neither that 2021 paper, nor the follow-up paper examining cocaine self-administration[23], determined whether any of the behavioral effects of photostimulation of NAc CRF neurons were driven by CRF release itself. Answering this question has recently been made more feasible by the publication of a CRF reporter mouse line demonstrating putative CRF neurons in the NAc of mice[24], opening up the use of a more genetically tractable animal model.

In this study, we thoroughly characterize accumbal CRF neurons and demonstrate a behavioral role for this population in instrumental learning. A significant portion of NAc CRF neurons are canonical SPNs enriched with SPN markers, projecting to both the ventral pallidum and ventral midbrain, and displaying canonical SPN electrophysiological and morphological properties. Interestingly, NAc CRF neurons are enriched for so-called "eccentric" SPN markers recently identified by Saunders and colleagues[14]. A significant proportion of NAc CRF neurons display low-threshold spiking (LTS) properties and morphology similar to neuropeptide Y (NPY)-containing LTS interneurons, yet do not express markers for LTS interneurons. We propose that these are non-canonical SPNs that have retained some of their immature electrophysiological properties. Finally, a small portion of CRF neurons display fast-spiking interneuron-like electrophysiological properties and gene expression (i.e., *Pthlh*, *Htr* and *Calb2*). Using fiber photometry methods, we find that accumbal CRF neurons show increased activity during reward seeking and that this activity scales depending on reward delivery. Importantly, CRF deletion from accumbal neurons facilitates faster acquisition of action-

outcome reward learning, but does not produce gross anhedonic changes. Together, these results provide the first in-depth transcriptional, anatomical, and electrophysiological characterization of NAc CRF neurons, demonstrating the heterogeneity of this population and identifying a role for accumbal CRF in the facilitation of action-outcome reward learning.

Results

Characterization of NAc CRF neurons using fluorescent in situ hybridization

Brains from male and female C57BL6/J mice were rapidly dissected and flash frozen. Using fluorescent in situ hybridization (ACD RNAscope Fluorescent Multiplex v1, v2) we performed a thorough assessment of co-localization for *Crh* mRNA with a variety of markers for SPNs (*Drd1, Pdyn, Drd2 and Penk*) and interneurons (*Chat, Npy, Sst, Th, Nos, Htr3, Calb2, Pthlh, Vip, Cck*). Collectively, these markers cover the preponderance of neuronal types in the NAc. Although we would prefer to assess protein, CRF antibodies are generally unreliable (particularly from run to run). Thus, it was not tractable to use immunohistochemical methods. Using this more reliable in situ hybridization method, we found that *Crh* mRNAs were present in 2.5% of NAc cells and 0.54% of dorsal striatal cells. There were no significant differences in *Crh*+ cells between the NAc shell and core or dorsomedial striatum and dorsolateral striatum (Figure S1a,b). We also found that there was a significant rostral-caudal gradient in *Crh*+ expression with caudal and middle regions of the NAc containing significantly more *Crh*+ cells compared to the rostral NAc (Figure S1c,d).

We found that the majority of *Crh*+ neurons expressed *Drd1* (66 ± 6%) or *Pdyn* (74 ± 3%), canonical markers for direct pathway SPNs. A smaller proportion of *Crh*+ neurons expressed *Drd2* (36 ± 5%) or *Penk* (24 ± 3%), canonical markers for indirect pathway SPNs (Figure 1a,b). *Crh*+ neurons constituted 3.0 ± 0.8% of all *Drd1*+ neurons and 1.2 ± 1.0% of all *Drd2*+ neurons (Figure 1c). We found minimal co-expression of *Crh* with striatal interneuron markers *Chat* (0.2 ± 0.1%), *Npy* (0.6 ± 0.2%), *Sst* (2.3 ± 0.5%), *Th* (0.7 ± 0.3%), *Nos* (1.0 ± 0.6%), *Vip* (1.2 ± 0.1%), *Hrt3* (2.5 ± 0.6%), *and Cck* (3.2 ± 0.4%) (Figure 1d). For *Calb2*, which encodes calretinin, there were small but appreciable percentages of co-expression with *Crh* (9.0 ± 1.2) (Figure 1d). *Pthlh*, a pan-

marker for a family of interneurons that includes parvalbumin-expressing fast-spiking interneurons, had similar co-expression with *Crh* mRNA (7.5% ± 1.2%) (Figure 1d). While there is not complete overlap, calretinin and Pthlh co-express in parvalbumin-expressing fast-spiking interneurons, suggesting that these are not entirely unique populations.

We next used the HiPlex RNAscope assay to determine if *Crh*+ neurons are either *Drd1*+ or *Drd2*+ only, or if they co-express these mRNAs. The HiPlex assay allows for visualization of up to 12 mRNA probes in the same tissue (Figure 1e). The majority of *Crh*+ neurons only expressed *Drd1*+ (51.1±1.6%) (Figure 1f). However, approximately half of *Crh*+ cells that co-expressed *Drd2*+ did so exclusively (10.6 ± 0.6%) while the other half of *Crh+/Drd2*+ cells also expressed *Drd1* (11.0 ± 1.7%).

A recent study by Saunders et al. (2018) identified a third classification of striatal SPNs they termed "eccentric" SPNs[14]. These eSPNs could be distinguished by the presence of one of four markers (*Otof, Tac2, Pcdh8* and *Cacng5*). We included these markers within our HiPlex design. We found that 69 ± 2% of *Crh*+ cells contained at least one "eccentric" marker, with a number of cells containing multiple "eccentric" markers (Figure 1g,h). In the NAc, 60 ± 1% of all *Drd1*+ neurons and 46 ± 2% of all *Drd2*+ neurons expressed at least one of these "eccentric" markers (Figure 1i). The number of CRF cells co-expressing eccentric markers was statistically greater at 69 ± 2% (one-way ANOVA with Sidak; main effect $F_{2,21} = 37.91$, $p < 0.0001$) than both *Drd1*+ and *Drd2*+ populations. These data indicate that, despite being a relatively small population, CRF cells overrepresent eccentric markers compared to canonical SPN populations.

NAc CRF neurons project to ventral pallidal and midbrain regions

We next wanted to understand the projection patterns of CRF neurons. To do so, we first performed double in situ hybridization for *Crh* and *Cre* mRNA in $Crh^{IRES\text{-}Cre/-}$ mice to assess the specificity and penetrance of Cre in the NAc in this line (Figure S2a). The specificity of this line (defined as the % of *Crh*+*Cre*+/total *Cre*+ cells) was very high (>85%) and similar in all regions analyzed: the paraventricular nucleus of the hypothalamus (95 ± 1%), NAc (88 ± 4%), BNST (93 ± 2%) and central amygdala (95 ±

4%) (Figure S2b). In contrast, the penetrance of Cre (defined as (%*Crh*+*Cre*)/total *Crh*) was significantly lower in the NAc (38 ± 4%) compared to the paraventricular nucleus (91 ± 1%), BNST (92 ± 2%) and central amygdala (78 ± 6%) (Figure S2c). Thus, while this Cre-driver line is specific for CRF neurons, it underrepresents the CRF population in the NAc. We decided to continue with this transgenic mouse line as it is the best currently available.

We next used a Cre-dependent viral vector in which GFP is expressed under the hSyn promoter to mark fibers of passage of transfected cells and mRuby is expressed under the synaptophysin promoter to mark where the fibers synapse (Addgene Cat# 71760). We packaged this plasmid into an AAV5 viral vector, which expresses well in the striatum[25]. We transduced this viral vector bilaterally into the NAc of *Crh*$^{IRES\text{-}Cre/-}$ mice. We then performed immunohistochemistry for tyrosine hydroxylase to identify midbrain dopamine neurons and substance P to delineate the ventral pallidum for quantification. We collected high power confocal images of the ventral pallidum and substantia nigra (*pars compacta* and *pars reticulata)*.

We found strong evidence for the presence of synaptic boutons in the ventral pallidum and in the substantia nigra *pars compacta/reticulata* based on the presence of GFP+ fibers and mRuby+ puncta (Figure 2a-c). We quantified the number of mRuby+ puncta present in the ventral pallidum versus the ventral midbrain using the criterion of 0.85–1.5 μm for a single synaptic bouton. We found significantly more mRuby+ puncta in the ventral pallidum compared to the midbrain (paired t-test, $p = 0.0165$) (Figure 2d). This finding is consistent with our in situ hybridization data indicating that CRF is present in a subset of both direct and indirect pathway SPNs, which project to the ventral pallidum. Only direct pathway SPNs project back to the midbrain, explaining the fewer mRuby puncta observed there. There is a dense lateral plexus within the striatum formed by SPN axon collaterals. Interestingly, we found evidence for mRuby+ varicosities along CRF-containing SPNs, indicating *en passant* axonal release sites (Figure 2e). Of note, there were several instances of CRF+ neurons expressed in clusters along the border of the NAc and ventral pallidum (Figure 2f).

Electrophysiological examination of NAc CRF+ neurons reveals three subtypes

Several studies have characterized the electrophysiological profile of different cell types within the striatum, using metrics of passive and active membrane properties: membrane resistance, membrane capacitance, resting membrane potential, action potential duration (at 50% repolarization), rheobase (minimum current injection required to elicit an action potential), subthreshold I-V slope (slope of the I-V curve at subthreshold potentials), F-I curves (spike frequency-current curves) and sag ratio (ratio between the steady state voltage following a hyperpolarizing step and the maximal voltage deflection following a hyperpolarizing step). While these properties have been most carefully studied in the dorsal striatum (see work by Tepper and colleagues[26-29]), work in the NAc is generally consistent with research done in the dorsal striatum. We assessed these active and passive properties in putative CRF+ neurons using two methods of labeling CRF neurons: *Crh*$^{\text{IRES-Cre/-}}$; Ai14 reporter mice (Figure S3a,b) and *Crh*$^{\text{IRES-Cre/-}}$ mice transduced with AAV5-DIO-eYFP viral particles during adulthood. The Ai14 reporter mouse was expected to show consistent expression across the NAc and did not require surgery, since this method labels cells that express CRF at any point in development. In contrast, the viral approach only targets cells that express CRF in adulthood, but has uneven expression based on the diffusion of viral particles and requires a surgical procedure. While there was a difference in distribution, nevertheless, we found three distinct types of electrophysiological profiles present in putative CRF neurons identified by the experimenters (Figure 3a). Thus, the data from both approaches was pooled for assessment of the electrophysiological properties of these three types.

Type 1, Type 2, and Type 3 CRF neurons displayed differences across a variety of metrics. Across all CRF+ cells analyzed, Type 3 neurons were less abundant in the NAc than Types 1 and 2 (Type 1: 46%, Type 2: 39%, Type 3: 15%) (Figure 3b). Type 1 cells had a greater membrane resistance compared to Type 2 and 3 neurons (Type 1: 565.4 ± 55.49 MΩ; Type 2: 235.1 ± 36.40 MΩ, Type 3: 160.4 ± 20.48 MΩ; one-way ANOVA, $F_{2,69} = 18.06$, $p < 0.0001$) (Figure 3c). Assessing action potential characteristics, we found that Type 3 neurons had a significantly shorter action potential duration compared to Type 1 or Type 2 neurons (Type 1: 1.23 ± 0.12 ms; Type 2: 1.27 ±

0.05 ms, Type 3: 0.70 ± 0.03 ms; one-way ANOVA, $F_{2,60} = 7.433$, $p = 0.0013$) (Figure 3d). Type 1 neurons had more depolarized resting membrane potentials (Type 1: -56.22 ± 1.196 mV, Type 2: -82.43 ± 1.018, Type 3: -81.03 ± 1.07; one-way ANOVA, $F_{2,69} = 82.64$, $p < 0.0001$), as well as a greater variance in resting membrane potentials (Bartlett's test, $p < 0.0001$). Type 2 and Type 3 cells had similar RMPs, which rested around the canonical RMP for SPNs (Figure 3c). Type 2 neurons had significantly larger membrane capacitance values than Type 1 or 3 (Type 1: 47.95 ± 3.61 pF; Type 2: 85.58 ± 3.41 pF; Type 3: 46.80 ± 3.53 pF; one-way ANOVA, $F_{2,69} = 35.54$, $p < 0.0001$) (Figure 3f).

In addition, there was a marked difference in the firing x current (F-I curve) relationship between Type 1, 2 and 3 cells (Figure 3g). Type 1 neurons almost always demonstrated depolarization-induced block of action potential firing at larger depolarizing current injections, whereas Type 2 and 3 neurons did not show similar accommodation or depolarization-induced block. Type 1 neurons also had a greater subthreshold IV slope (passive conductance) compared to Type 2 and 3 neurons (Type 1: 0.3556 ± 0.0265 mV/pA, Type 2: 0.07879 ± 0.00376 mV/pA, Type 3: 0.09045 ± 0.008394 mV/pA; one-way ANOVA, $F_{2,69} = 60.74$, $p < 0.0001$) (Figure 3h). Finally, Type 1 neurons had a significantly lower rheobase compared to Types 2 and 3 (Type 1: 58.48 ± 5.68 pA, Type 2: 246.4 ± 17.8 pA, Type 3: 284.1 ± 30.78 pA; one-way ANOVA, $F_{2,69} = 65.36$, $p < 0.0001$) (Figure 3i). The greater subthreshold IV slope and decreased rheobase are likely explained by the increased membrane resistance observed in Type 1 neurons.

Following experimenter determined classification of cells as Type 1, 2, or 3, we performed two unsupervised approaches to validate our categorization of NAc CRF neurons. First, using our eight different electrophysiology parameters, we used principal component analysis to perform dimensionality reduction and better visualize our data. Retaining principal components (PCs) with eigenvalues of at least 1, we found that two PCs explained 78.71% of the variance in the dataset. Of these two PCs, the majority of CRF neuron electrophysiology properties loaded onto PC1 (membrane resistance, resting membrane potential, membrane capacitance, F-I curve slope, sag ratio, and rheobase) and comprised 50.69% of variance, while action potential duration and

maximum firing frequency loaded predominantly onto PC2 and comprised 21.09% of the variance in the dataset. Visualizing CRF neurons colored by experimenter-determined Type I, 2 and 3 (Figure 3j), we observed that Type I and Type 2 neurons were differentiated mainly along PC1, while PC2 mainly differentiated Type 2 and 3 neurons based on maximum firing rate and action potential duration. However, there was some co-mingling particularly between different types, indicating a degree of overlap between CRF neuron types. We next performed unsupervised clustering of our electrophysiology dataset using hierarchical clustering with Ward's linkage method. The results showed that several Type 1 and even some Type 3 neurons became clustered with Type 2, indicating that a classification approach based on dorsal striatal electrophysiological profiles may not be entirely applicable to the NAc and, in particular, to this CRF population (Figure S4).

Morphological profile of accumbal CRF neurons

In a separate set of experiments, we included biocytin in our recording solution so that we could look at the morphological properties of Type 1, 2 and 3 CRF neurons using high power confocal imaging (Figure 4a). First, we performed a Sholl analysis. Type 1 neurons had significantly fewer intersections than Type 2 or 3 neurons (two-way repeated measures ANOVA, length x type interaction, $F_{28,266} = 2.501$, $p < 0.0001$) (Figure 4b). Likewise, Type 1 neurons had a smaller cumulative dendritic length compared to Type 2 and 3 neurons (Type 1: 1398 ± 227 μm; Type 2: 3112 ± 334 μm; Type 3: 2508 ± 253 μm, one-way ANOVA, $F_{2,19} = 9.413$, $p = 0.0014$) (Figure 4c). There was no significant difference in soma size (one-way ANOVA, $F_{2,20} = 0.5341$, $p = 0.5943$) (Figure 4d). Finally, Type 2 neurons had a greater spine density than Type 1 or 3 (Type 1: 0.15 ± 0.03 spines/μm; Type 2: 0.72 ± 0.07 spines/μm; Type 3: 0.21 ± 0.03 spines/μm, one-way ANOVA, $F_{2,18} = 33.97$, $p < 0.0001$) (Figure 4e).

Based on the literature[29,30] and our electrophysiological and morphological analysis, we conclude that Type 3 neurons are fast-spiking interneurons. This is consistent with our in situ hybridization data indicating that a small percentage of CRF neurons express *Pthlh* and *Calb2*. Furthermore, we also conclude that Type 2 neurons are SPNs, based on both the electrophysiological and morphological data that is

consistent with the past literature[31]. This is consistent with our findings that ~80% of *Crh*+ neurons in the NAc express either *Drd1* or *Drd2*, and that NAc CRF neurons project primarily to the ventral pallidum and substantia nigra, canonical target regions of SPNs. However, it is difficult to categorize the Type 1 NAc CRF neurons. Functionally and structurally, Type 1 neurons resemble LTS interneurons. However, co-expression of *Crh* mRNA with markers of known LTS populations (i.e., *Npy, Sst, Th, Htr3*[26,28,29,32]) was negligible, making it highly unlikely that the Type 1 neurons we identified here belong to any of those interneuron populations.

Development trajectory of Drd1+ accumbal neurons

There were differences in the proportion of Type 1, 2 and 3 neurons between Ai14 tdTomato+ cells from *Crh*$^{\text{IRES-Cre/-}}$; Ai14 mice and virally transduced eYFP+ cells from *Crh*$^{\text{IRES-Cre/-}}$ mice, indicating a potential shift in relative expression throughout development (X^2 test, $p = 0.0255$) (Figure S3c). In addition, in the dorsal striatum it has been shown that D1-expressing SPNs alter their electrophysiological and structural profile during development such that early in development (postnatal day 9–17) SPNs are markedly more excitable and have fewer spines and reduced dendritic length[32]. Since we could not readily attribute Type 1 neurons to any one class of interneurons, we hypothesized that Type 1 neurons are direct pathway SPNs that retain their initial excitable profile into adulthood. To test this, we compared several key electrophysiological components of D1+ neurons recorded from juvenile (P12–20) *Drd1*^{tdTomato} mice to adult Type 1 and Type 2 CRF neurons (Figure 5a). Juvenile D1+ neurons exhibited a phenotype that is essentially “in between” the properties of adult CRF Type 1 and Type 2 neurons.

Juvenile D1+ neurons had an average membrane resistance (R_M) most similar to adult Type 2 CRF neurons, with significantly lower membrane resistance than adult Type 1 cells (Juvenile D1+: 228 ± 37 MΩ, Type 1: 565 ± 55 MΩ, Type 2: 235 ± 36 MΩ, one-way ANOVA with Dunnett’s post-hoc t-test, $p < 0.05$) (Figure 6b). The resting membrane potential (RMP) and rheobase of juvenile D1+ neurons was significantly different from both adult Type 1 and Type 2 CRF neurons. Juvenile D1+ neurons displayed an in between phenotype in both these measures. The RMP of juvenile D1+

neurons was significantly lower than that of adult Type 1 CRF neurons, but was significantly higher than the RMP of adult Type 2 CRF neurons (Juvenile D1+: -74 ± 3 mV, Type 1: -56 ± 2 mV, Type 2: -82 ± 1 mV, one-way ANOVA with Dunnett's post-hoc t-test, $p < 0.05$) (Figure 5c). The rheobase of juvenile D1+ neurons was significantly higher than that of adult Type 1 CRF cells and significantly lower than adult Type 2 CRF cells (Juvenile D1+: 105 ± 12 pA, Type 1: 58 ± 6 pA, Type 2: 246 ± 18 pA, one-way ANOVA with Dunnett's post-hoc t-test, $p < 0.05$) (Figure 5d). While the membrane resistance of juvenile D1+ neurons more closely resembled that of adult Type 2 CRF neurons, the membrane capacitance of juvenile D1+ neurons was more similar to the capacitance of adult Type 1 CRF neurons. The membrane capacitance of juvenile D1+ neurons was significantly lower than that of adult Type 2 neurons, but not significantly different from Type 1 neurons (Juvenile D1+: 54 ± 4 pF, Type 1: 48 ± 4 pF, Type 2: 86 ± 3 pF, one-way ANOVA with Dunnett's post-hoc t-test, $p < 0.05$) (Figure 5e). These findings are consistent with the notion that there are fewer spines and therefore less overall surface area in immature D1+ neurons compared to fully mature SPNs. Finally, the subthreshold IV slope of juvenile D1+ cells was significantly different from that of both adult CRF neuron groups, displaying an intermediate phenotype. Adult Type 1 CRF neurons had a significantly higher slope than juvenile D1+ neurons, while adult Type 2 CRF neurons had a significantly lower slope than juvenile D1+ neurons (Juvenile D1+: 0.199 ± 0.023 mV/pA, Type 1: 0.356 ± 0.027 mV/pA, Type 2: 0.079 ± 0.004 mV/pA, one-way ANOVA with Dunnett's post-hoc t-test, $p < 0.05$) (Figure 5f). Our unsupervised hierarchical clustering analysis found several subclusters containing a mix of Type 1 and Type 2 cells, which may indicate that some CRF+ cells maintain a juvenile phenotype (Figure S4).

NAc CRF-containing neurons track outcomes in operant learning task

It has recently been shown that optogenetic stimulation of CRF+ cells in the rat NAc is sufficient to sustain intracranial self-stimulation and promotes the incentive salience of sucrose reward[17]. However, the dynamics of this NAc CRF population activity during effortful reward learning has not been studied. To do this, we transduced AAV5-FLEX-GCaMP6s into the NAc of *Crh*$^{\text{IRES-Cre/-}}$ mice and implanted optical fibers unilaterally into

the same location (Figure 6a). Animals were food restricted and trained on a simple FR1 operant task for food pellet reward. During training, mice were tethered with patch cables every day and recorded every other day (Figure 6b). Once mice met criteria on an FR1 schedule (defined as at least 30 rewards per session with 75% active side discrimination) for 3 consecutive days, they were moved to FR3. Mice were run on FR3 until criteria (30 rewards, 75% discrimination) was met for at least 3 consecutive days. On average, mice took 5 days to meet criteria on both FR1 and FR3 (Figure 6c). On days when criteria was met, nose poke discrimination was >90% for both FR1 and FR3 (Figure 6d). We aligned calcium signals to TTLs evoked by head entries into the reward magazine. The open-source fiber photometry analysis tool GuPPy developed by the Lerner lab was used for analysis[33]. Standard z-scores were calculated across the whole recording session using an isosbestic control channel (405 nm) but no baseline correction. Z-scores were aligned with behavioral events using infrared beam-evoked TTL timestamps.

Measuring the integrated calcium activity of the NAc CRF+ neuronal population, we found a robust increase in activity at the time of magazine head entry for both rewarded and unrewarded entries (Figure 6e). We then used the fluorescence z-scores to calculate the area under the curve (AUC) within 2.5s time bins around the magazine head entry TTLs. We found that there was a significant difference in the fluorescence elicited by rewarded verses unrewarded head entries (two-way ANOVA with Sidak post-hoc; main effect of time $F_{13,19} = 18.12$, $p < 0.001$; group $F_{1,7} = 5.362$, $p = 0.0537$; time x group $F_{13,91} = 5.488$, $p < 0.0001$) (Figure 6f). Rewarded head entries elicited significantly more activity immediately following magazine entry (0 to 2.5s from TTL) compared to unrewarded head entries. Interestingly, this increased activity in response to rewarded head entries was followed by a significantly greater depression in activity which persisted for several seconds (5 to 15 s from TTL). This significant dip in activity following magazine head entry corresponded with the approximate time of reward consumption. In addition to the difference in AUC, we found that the peak fluorescence immediately following magazine head entry (0 to 2.5s) was greater for rewarded head entries compared to unrewarded head entries across all animals (paired t-test, $p = 0.0002$) (Figure 6g). In order to investigate the dynamics of NAc CRF activity across

training, we examined the activity in response to rewarded magazine entries on early and late FR1 days (Figure S5a). While rewarded head entries in both early and late FR1 days elicited a robust increase in activity following magazine entry, there appeared to be slight differences in the post-reward inhibition (Figure S5b,c). Although not significant, there was a trend of increased suppression in later FR1 days verses early FR1 days (Figure S5d). This suggests that NAc CRF activity may develop across training, but the present study is not able to parse this phenomenon further. Thus, we concluded that this population of NAc neurons is sensitive to action outcomes and is most active during the motoric acquisition of the reward.

The role of NAc CRF release in action-outcome reward learning

We next wanted to determine the role of CRF peptide release from NAc neurons during this same operant task. To test this, we utilized a mouse line with loxP sites flanking the CRF allele (*Crh*$^{loxP/loxP}$) (Figure S6a), generated and validated at the University of Washington[34]. To conditionally knock out CRF peptide from NAc neurons, *Crh*$^{loxP/loxP}$ mice were transduced with either AAV5-CMV-Cre-eGFP (CRF cKO) or AAV5-CMV-eGFP (control) bilaterally into the NAc. We first confirmed CRF deletion using RT-qPCR in a cohort of *Crh*$^{loxP/loxP}$ mice injected with control (GFP) or CRF cKO (GFP-Cre) virus (Figure S6b). There was a significant decrease in NAc *Crh* mRNA expression in CRF cKO mice compared to controls (Figure S6c). We also confirmed that this manipulation did not affect baseline corticosterone levels (as a proxy for hypothalamic-pituitary-adrenal axis function) or produce gross changes in body weight (Figure S6d,e). We then prepared a cohort of control and CRF cKO mice for behavioral testing. Following behavioral testing, we confirmed knock-down in these animals with in situ hybridization, probing for *Crh, Cre* and *Gfp* mRNA in the NAc. As expected, CRF cKO mice were positive for *Cre* mRNA within the *Gfp*+ viral plume and had disrupted *Crh* mRNA expression. In contrast, control mice had no *Cre* mRNA expression within the *Gfp* plume and had normal *Crh* mRNA expression (Figure 7a). The knockdown of NAc *Crh* within the injection bolus of CRF cKO mice was significant, with an average of 46 cells in GFP control mice and 9 cells in CRF cKO mice (Mann-Whitney, $p = 0.0027$), an 80%

reduction (Figure 7b). Thus, our manipulation resulted in a chronic and stable knock-out in adult mice.

In our operant task, we found that CRF deletion from NAc neurons in adulthood resulted in a faster time to reach criteria for FR1, which did not persist to FR3 training (two-way repeated measures ANOVA with Sidak's; main effect of FR schedule: $F_{1,12}$ = 4.900, p = 0.047; group: $F_{1,12}$ = 4.900, p = 0.0470; and FR schedule x group: $F_{1,12}$ = 4.900, p = 0.0470) (Figure 7c). Nose ports were baited with food for the first three days to encourage interaction with the nose ports, and those days were excluded from analysis. During the first unbaited FR1 training day, CRF cKO mice had quicker reward acquisition (two-way repeated measures ANOVA with Sidak's; main effect of time: $F_{6,72}$ = 51.21, p < 0.0001; group: $F_{1,12}$ = 8.242, p = 0.0141; time x group: $F_{6,72}$ = 4.804, p = 0.0004) (Figure 7d). As some mice did not reach criteria on the first unbaited day, we also compared reward acquisition over session time on the first day criteria was reached, and found that CRF cKO mice were quicker to acquire rewards at the beginning of training even when all mice were reaching criteria (two-way repeated measures ANOVA with Sidak's; main effect of time: $F_{6,72}$ = 140.0, p < 0.0001; and time x group: $F_{6,72}$ = 2.933, p = 0.0129) (Figure 7e). This effect did not persist across subsequent days, and there was no difference in overall nose pokes between groups on any day (Figure S7a). Thus, deletion of CRF from the NAc appears to promote quicker initial acquisition of operant reward learning.

In line with our data showing an initial difference in speed of reward acquisition, control mice significantly reduced their time to earn 10 rewards between the first day criteria was reached on FR1 and the third day (paired t test, p = 0.014). In contrast, CRF-cKO mice had an initially shorter time to 10 rewards that did not differ between FR1 and FR3 phases (paired t test, p = 0.204) (Figure 7f). Following the last day of FR3 criteria, mice were tested on a progressive ratio schedule that is thought to probe for motivational drive[35], but showed no difference between groups in breakpoint or time to earn rewards (Figure S7b,c). Taken together, these data demonstrate that CRF deletion from NAc neurons enhances action-outcome acquisition, indicating that under normal conditions, CRF release from NAc neurons acts to constrain action-outcome acquisition.

In the operant experiments, CRF cKO mice seemed to learn more quickly about action-outcomes in reward-seeking. To assess if deletion of CRF peptide from NAc neurons produced a hedonic-like effect in our experimental setup, we analyzed sucrose preference in control and CRF cKO mice. Birnie et al. (2023) found a pronounced sex difference in their studies, with effects only being prominent in males. Thus, for this set of studies we fully powered experiments to assess the effect of CRF manipulation in male versus female mice.

Mice were separated into individual cages equipped with two bottles and acclimated with water only for 4 days. Following acclimation, one bottle was filled with 1% sucrose and the other with water (Figure 7g). Daily bottle weights were used to calculate sucrose preference as the percent total daily intake that was sucrose. We first analyzed males and females separately and found no significant differences between control and cKO males (Figure S7d) or females (Figure S7e). We then pooled the data but found no difference in sucrose preference between control and CRF cKO mice (unpaired t-tests corrected for multiple comparisons by Sidak-Bonferroni; day 1, $p_{adj} > 0.999$; day 2, $p_{adj} = 0.902$; day 3, $p_{adj} = 0.998$) (Figure 7h). There was also no difference in daily total intake (sucrose+water) between groups (unpaired t-tests corrected for multiple comparisons by Sidak-Bonferroni; day 1, $p_{adj} > 0.818$; day 2, $p_{adj} = 0.986$; day 3, $p_{adj} = 0.880$) (Figure 7i). These data indicate that there are no gross differences in hedonic drive or general consummatory behavior between control and CRF cKO mice. Thus, this further indicates that the improved performance of CRF cKO mice in the operant task is specific to acquisition of action-outcome behavior, rather than a byproduct of changes to the hedonic quality of reward.

It is also possible that CRF release from NAc neurons promotes exploration in novel environments, diminishing attention from specific tasks[18-22]. While we did not video monitor activity in the operant chambers, these same animals were exposed to a novel open field prior to operant training. We found that deletion of CRF of NAc neurons reduced locomotion in response to a novel environment during the first minute (unpaired t-test, $p = 0.0120$) (Figure 7j-l), presumably when the novelty is greatest, but did not affect locomotion in subsequent minutes after habituation had taken place (unpaired t-test, $p = 0.6725$) (Figure 7m). This is consistent with previous work demonstrating that

CRF receptor antagonism in the NAc depresses novelty exploration[19] and locomotion[36]. CRF invigoration of motor behaviors in the face of novelty may, in part, explain the inhibition of goal-directed behaviors such as nose-poking for reward.

Discussion

In this study, we comprehensively characterized the structure and function of CRF-expressing neurons in the NAc and provide evidence that this population constrains action-outcome acquisition during reward learning. To our knowledge, the neurochemical and physiological identity of these neurons has never been described, nor has the behavioral role of CRF release itself from these neurons. Here we show that CRF neurons are significantly more abundant in the NAc compared to the dorsal striatum. We also show that there is a gradient of CRF expression, with lower levels expressed in the rostral NAc and increasing abundance in mid- to caudal NAc. We demonstrate that CRF-containing neurons in the NAc are primarily D1- and D2-containing SPNs that project both to the ventral pallidum and back to the midbrain, and have canonical and non-canonical electrophysiological and morphological phenotypes associated with SPNs. While CRF expression was found in both direct and indirect pathway SPNs, it was most prominently expressed in dynorphin+ direct SPNs. In general, it appears that “eccentric” SPN markers are more abundant in the NAc than in the dorsal striatum. Regardless, NAc CRF+ neurons are enriched for four of these “eccentric” transcripts (*Otof, Tac2, Cacng5* and *Pcdh8*) compared to NAc SPNs as a whole.

We monitored the activity patterns of NAc CRF neurons during an operant conditioning task and found that CRF-containing neurons increase their activity during both unrewarded and rewarded head entries, but the integrated calcium response was greater for rewarded head entries. Furthermore, there a significant depression in activity only following rewarded head entries, peaking at 5 seconds after the head entry. Thus, CRF neuronal activity tracks both reward-seeking actions and salient outcomes. Finally, conditional CRF deletion enhanced the acquisition of the instrumental task and increased the number of rewards acquired during the initial acquisition phase. These findings indicate that under normal conditions, CRF release from this sparse population

of NAc neurons constrains reward acquisition at a period when we speculate the environment is most novel and uncertain. This interpretation is supported by the decreased locomotion exhibited by the CRF cKO mice during the first minute of an open field, suggestive of decreased exploration of a novel environment. To our knowledge, these data are the first report of the behavioral function of CRF release from NAc CRF neurons. Furthermore, this was a surprising finding given the recent optogenetic interrogation of these neurons and since activity of direct pathway SPNs in the NAc are thought to promote reward acquisition[37,38]. Taken together, this study identifies a novel and unique peptidergic cell population within the NAc that plays a critical role in shaping action-outcome learning.

CRF neurons in the NAc are comprised of a heterogenous population of SPNs and fast-spiking interneurons.

There have been no studies to date profiling the cellular properties of NAc CRF+ neurons despite the extensive characterization of SPNs and interneurons in the striatum. Therefore, our goal was to apply neurochemical, structural, and electrophysiological approaches to describe NAc CRF+ neurons. The vast majority (70–85%) of CRF cells expressed canonical SPN markers with a small percentage displaying the fast-spiking interneuron neurochemical phenotype. Analysis of projection patterns supported the neurochemical data. These data alone advance our understanding of CRF+ neurons in the striatum, as it has been presumed that these neurons produce their behavioral output through local connections. Since SPNs send projections outside the NAc while also maintaining a dense lateral plexus via axon collaterals, they can influence both local circuit function and long-range projection regions.

However, our electrophysiological and morphological characterization of NAc CRF+ neurons challenges the current striatal cell classification system that was developed primarily in the dorsal striatum. It is clear that a portion of CRF-containing neurons display canonical SPN electrophysiological properties and a small proportion display fast-spiking interneuron-like properties consistent with the neurochemical and projection data. But approximately half of the Cre+, putative CRF-containing cells in our

preparation, displayed a non-canonical SPN electrophysiological and morphological phenotype more characteristic of low-threshold spiking interneurons (i.e. NPY-, SST-, 5-HT3- and TH-containing interneurons). This was in direct contrast to our neurochemical examination, which found negligible expression of these markers in NAc *Crh*+ neurons.

To this, we make three points. First, direct pathway SPNs do display low-threshold spiking properties and aspiny features early in development[32]. We find that Type 1 and Type 2 CRF neurons recorded from adult mice share electrophysiological features with D1-containing direct SPNs recorded from juveniles. It is possible that some portion of direct SPNs, perhaps those expressing so-called “eccentric” markers, retain some of their “immature” properties in the NAc. Second, the electrophysiological phenotypes we identify here in the NAc are similar to what has been reported for CRF+ neurons in the BNST. It remains a point of debate whether the NAc is part of the striatum, part of the extended amygdala or its own unique region. Considering that at least portions of the NAc (NAc shell) are considered by some to be part of the extended amygdala[3], it is worth considering the electrophysiological properties of BNST CRF neurons. In 2013, Winder and colleagues identified two types of BNST CRF neurons that had low-threshold spiking properties and one type that displayed canonical SPN-like properties[39], similar to our results here. It is possible that developmentally, NAc CRF neurons retain the electrophysiological features of their BNST counterparts. Finally, an unsupervised hierarchical clustering analysis re-classified a portion of Type 1 and Type 3 cells with the Type 2 neurons. This result suggests that a priori definitions of cell types developed in other brain regions (i.e. dorsal striatum) may not hold up when applied to categorization of NAc CRF neurons. Furthermore, there may additional defining properties of neuronal subtypes that we are not yet measuring or are unable to measure.

Accumbal CRF neuronal activity tracks and shapes action-outcome during reward learning

Here we demonstrate that deletion of CRF enhances acquisition of instrumental reward learning, particularly early in training, indicating that under normal conditions CRF acts to constrain action-outcome learning. This effect was not due to a difference in hedonic

perception or motivational drive since CRF cKO mice show normal sucrose preference and show no difference in a progressive ratio task once fully trained. We did find that CRF promotes exploratory behavior in response to a novel open field environment.

Based on our anatomical data, accumbal CRF neurons are one of several sources of CRF to the NAc, ventral pallidum and ventral midbrain. We originally hypothesized that deletion of CRF would impair reward learning and action-outcome performance in food restricted animals based on work demonstrating that exogenous CRF application enhances acetylcholine and dopamine transmission in the NAc and facilitates appetitive behaviors[17,19-21,40]. We have disproven this original hypothesis and instead offer two potential interpretations of our data.

"Throw caution to the wind…"

First, we suggest that CRF, as a stress-associated neuropeptide, is suppressing food acquisition and consumption in the context of an instrumental learning task during a period in the task where the environment is most novel and most stressful. The antagonistic relationship between stress and feeding (i.e., stress-induced hypophagia) in rodents has been well described[41]. Indeed, a classic stress-induced anxiety measure is novelty-induced suppression of feeding. Stress-induced hypophagia is often attributed in part to CRF neurons in the hypothalamus modulating feeding-associated neurons in the arcuate nucleus[41]. However, it is possible that in the context of reward learning, CRF from this sparse population of NAc neurons constrains initial acquisition in the face of high novelty by tempering the "go" signal from direct pathway SPNs, which is thought to potentiate and reinforce behaviors[7,42]. CRF is generally an excitatory transmitter; both CRF receptors couple to either Gαs or Gαq and, therefore, would potentially counteract inhibitory GABA release from SPNs[43]. This may be the case particularly when both the effort and reward payoff is low. Bryce and Floresco demonstrated that intra-NAc microinfusion of CRF reduces action-outcome performance under low effort/risk, low reward conditions (like our task), but increases the performance under high risk, high reward conditions[44]. Unfortunately, there is a dearth of information on the function of CRF in the ventral pallidum and ventral midbrain, particularly in the context of reward processing, so this interpretation is fairly speculative.

"Keep your head on a swivel…"

A second possible interpretation of our findings is that CRF enhances exploratory behavior thus limiting focus on one specific task, especially early in task acquisition. Exogenous application of CRF into the NAc enhances motor behavior, while inhibition of CRF receptors in the NAc or deletion of CRF receptors from dopamine neurons inhibits exploration of novel objects[19,36]. Here we find that deletion of CRF from accumbal neurons reduces locomotor responses to a novel environment, consistent with previous findings. The notion that CRF enhances cognitive flexibility by enhancing exploration or environmental surveillance has been put forward in the context of CRF excitation of noradrenergic locus coeruleus neurons that project to the prefrontal cortex[45]. A similar role for CRF has been assigned to CRF modulation of serotonin[45]. It is possible that CRF regulation of accumbal, pallidal and midbrain function may infuse some flexibility in engaging and disengaging with reward learning that is absent following deletion of CRF from NAc neurons.

Concluding Remarks

In conclusion, this study elucidates a novel role for CRF in regulating action-outcome learning when released from a sparse subpopulation of accumbal SPNs. It is remarkable that despite only representing 2-3% of NAc neurons, this CRF population can exert significant effects on NAc-dependent reward learning behavior. Future studies will continue to probe the role of these neurons in modulating appetitive processing for both natural rewards and drugs in male and female mice.

Methods

Animals: All procedures were done in accordance with the University of Minnesota Animal Care and Use Committee. Both male and female mice were used in approximately equal numbers, ages post-natal day 60-224, unless otherwise specified. Mice were group housed in specific-pathogen free conditions under a 16h light cycle (6:00 ON/20:00 OFF) with freely available food and water; “summer” photoperiods to facilitate breeding. Two weeks prior to experimental testing, mice were transferred to investigator managed standard housing and kept under a 12h light cycle (6:00 ON/18:00 OFF) for the remainder of testing. Unless otherwise noted, food and water

were available ad libitum. For in situ hybridization experiments, C57BL/6J mice (JAX stock: 000664) were used. For viral tracing experiments, *Crh*$^{IRES\text{-}Cre/-}$ mice (JAX stock: 012704) were used. For electrophysiology and fiber photometry experiments, *Crh*$^{IRES\text{-}Cre/-}$ mice were crossed with Ai14 (JAX stock: 007914) reporter mice. For CRF conditional knockout experiments, *Crh*$^{loxP/loxP}$ mice generated by Dr. Michael S. Clark and validated by Dr. Larry Zweifel at the University of Washington were used.

Rigor and Reproducibility: *Blinding*: When possible, experimenters directly performing the experiments were blinded to animal conditions: experimental or control.
Automation: Wherever possible, we used automated systems to acquire and analyze our data. *Power analyses* were used determine sample sizes using G*Power 3.1[46,47]. The power analysis is based on the expected magnitudes and SDs of results based on our prior data and previous literature as well as an α-value of 0.05. Of note, for the majority of experiments, we did not fully power our experiments to assess sex-differences. In the future we are analyzing potential trends and conducting fully powered sex-difference experiments.

Fluorescent in situ hybridization (RNAscope, ACD): Mice were anesthetized with isoflurane and rapidly decapitated. Brains were extracted and flash-frozen in isopentane on dry ice. Brains were stored at -80°C until sectioning. Prior to sectioning, brains were moved to -20°C and acclimated for 2–24 hours. Using a Leica CM8060 cryostat, 16µm slices were thaw mounted onto slides (Superfrost, Fisher) and stored at -80°C until assayed. RNAscope manual fluorescent multiplex v1, multiplex v2, and HiPlex assays were run as detailed in ACD technical manuals and previously reported (see https://acdbio.com/main-category/user-manuals)[40]. For multiplex v1 and v2 experiments, markers were run separately (Figure 1b-d). For all in situ hybridization experiments, N represent animals with approximately equal number of male and female. For v2 assays, we used Opal fluorophore reagent packs: 488, 520, 570, 620 and 780 (Akoya Biosciences). The following probes were purchased from ACD: Mm-Drd2-T1, Mm-Drd1-T2, Mm-Crh-T3, Mm-Otof-T4, Mm-Pcdh8-T5, Mm-Cacng5-T6, Mm-Tac2-T7, Mm-Crh-C1, CRE-C2, EGFP-C3, Mm-Vip-C2, Mm-Cck-C2, Mm-Nos1-C2, Mm-SST-C2,

Mm-Npy-C2, Mm-Meis2-C2, Mm-Drd1-C2, Mm-Drd1-C3, Mm-Htr3a-C2, Mm-Calb2-C2, Mm-Chat-C3, Mm-Pdyn-C3, Mm-Drd2-C3, Mm-Penk-C3, Mm-Th-C2.

Imaging and analysis: Tissue was imaged using a Keyence BZ-X710 fluorescence microscope or a Leica Stellaris 8 confocal microscope. For viral tracing experiments: 20x tile images of sagittal sections were taken, with additional 63x oil immersion, zoom 2 z-stacked and tiled images of regions of interest. Puncta were quantified using FIJI/ImageJ particle counter. For RNAscope experiments: 20x tiled images of the NAc were captured. For each run of RNAscope, capture settings were identical across animals. Settings were adjusted as needed between runs. DAPI expression was used to align images from separate HiPlex rounds as needed; this was done in Adobe Photoshop. For analysis, HALO image analysis platform (Indica Labs) was used. The NAc was either delineated by atlas overlay using the ABBA FIJI/ImageJ plugin (BIOP, https://biop.github.io/ijp-imagetoatlas) or for HiPlex experiments, outlined by hand. DAPI expression was used to delineate cells, and RNA puncta were quantified using the HALO FISH-IF module. For each probe, the threshold for minimum intensity, puncta size and number of puncta was titrated based on signal quality and expression pattern. The same analysis settings were applied across all sections from a single RNAscope run. For morphological analysis FIJI/ImageJ plugins Dendritic Spine Counter and Neuroanatomy were used.

Stereotaxic surgeries and viral vectors: Adult mice were quickly and deeply anesthetized using isoflurane (4% induction, 2% maintenance), and the skull leveled on a stereotaxic frame (Kopf, Model 1900). Viral particles were delivered using handmade 30g metal injectors connected to a 2uL syringe (Hamilton) with polyethylene tubing and delivered via pump (WPI microinjection syringe pump) at 100nL/min. For some experiments we also use glass sharp electrodes and Drummond Nanoject II microinfusion system. The injector was lowered to the appropriate depth and left to settle for one minute before beginning injection; following injection, the injector was left at depth for at least 5 minutes before the injector was slowly removed. For viral tracing experiments, either AAV5-hSyn-FLEx-GFP-2A-Synaptophysin-mRuby (Addgene

plasmid #71760 gifted by Liqun Luo[48], virus packaged by UMN Viral Vector and Cloning Core) viral particles were delivered into the NAc (AP = 1.15, ML = ±1.1, DV = 4.7; mm relative to bregma; 200nL) of *Crh*$^{IRES\text{-}Cre/-}$ mice. For some of the electrophysiology experiments, *Crh*$^{IRES\text{-}Cre/-}$ mice were injected with AAV5-Ef1a-DIO-eYFP (AP = 1.2, ML = ±1.1, DV = 4.75; 300nL). For CRF conditional knockdown experiments, intracranial injections were done as described with either AAV8-CMV-eGFP-Cre-WPRE-SV40 (Addgene viral prep #105545-AAV8 gifted by James M. Wilson) or AAV8-CMV-eGFP-WPRE (Addgene viral prep #105530-AAV8 gifted by James M. Wilson), bilaterally into the NAc (AP = 1.2, ML = ±1.1, DV = 4.75; 300nL) of *Crh*$^{loxP/loxP}$ mice. For fiber photometry experiments, intracranial injections were performed alongside fiber implantation. *Crh*$^{IRES\text{-}Cre/-}$*; Ai14* mice were injected with AAV5-Syn-FLEx-GCaMP6s-WPRE (Addgene viral prep #100845-AAV5 gifted by Douglas Kim and GENIE Project[49]) unilaterally into the NAc (AP = 1.3, ML = ±1.3, DV = 4.7; 300nL), and a fiber-optic cannula (Doric, MFC_400/430-0.66_5mm_MF2.5_FLT) was placed dorsal to the injection bolus (DV = -4.3). Analgesic (carprofen, 5mg/kg s.c.) was given prior to and for 3 days after surgery.

Immunohistochemistry: Mice were intracardially perfused with PBS containing 10U/mL Heparin until the liver cleared (approximately 5 minutes) followed by 40 ml fixative solution (4% paraformaldehyde; 4% sucrose in 0.1M PB) at 3 ml/min. Brains were incubated in 30% sucrose (in 0.1 M PB) for 24 h at 4 °C and sliced with a cryostat or microtome. 40µm floating sections were washed in PBS and then blocked for 1hr in 5% normal goat serum or donkey serum, 0.3% Triton-X in PBS at RT. Sections were then incubated in primary antibody for 12-18hrs at RT (Rat anti-Substance P, 1:400, EMD Millipore, Cat # Mab356; Chicken anti-TH, 1:1000, Aves Laboratories, Cat # TYH). Slices were incubated in goat or donkey Alexa Fluor secondary antibodies (1:500, Invitrogen) for 2 hr at RT. For TH immunoreactivity, slices were incubated in Goat anti-Chicken Biotin (1:500) for 2 hr RT and then Streptavidin-700 (1:500) for 1.5 hr RT. Slices were washed 3 x 10 min in PBS, then 2 x 10 min, mounted and coverslipped. Images (1024x1024) were acquired using a confocal microscope (Stellaris 8 Confocal microscope). Three to five confocal images were acquired per region (ventral pallidum, ventral

midbrain) per mouse, with 5 mice total. Analysis was performed using ImageJ software on acquired images.

Ex vivo electrophysiology Adult (8-20 week-old) *Crh*$^{IRES\text{-}Cre/-}$*; Ai14* mice were anesthetized using isoflurane, rapidly decapitated and brains quickly extracted for sectioning. Coronal 240 µm slices were cut on a vibratome (Leica VT1200S) in ice cold cutting solution. Slices were allowed to recover in warm (33°C) oxygenated artificial cerebrospinal fluid (ACSF) for 30-60 min before the recovery chamber was removed from the warm water bath and maintained room temperature for the remainder of the recording day. For electrophysiology experiments, slices were transferred to the recording chamber maintained at physiological temperature (30-32°C) in the recording chamber. A gigohm seal was achieved before achieving whole-cell configuration using electrodes (2-5MΩ) filled with a $KMeSO_4$ internal solution. In whole-cell current clamp, passive membrane properties were recorded. A current-step protocol (-120 to +360pA, 40pA steps) was applied to examine the firing properties of these cells. Data were acquired at 5 kHz and filtered at 1 kHz using Multiclamp 700B (Molecular Devices) or Double IPA (Sutter Instruments). Data were analyzed using pClamp (Molecular Devices) or SutterPatch (Sutter Instruments). In a subset of cells, 1% biocytin was included in the internal solution. These cells were fixed in 4% paraformaldehyde (PFA) for at least 24 hrs following recording, then post-hoc stained for streptavidin (Invitrogen, S32353) and imaged (Leica Stellaris 8, 63x). Measures of dendritic length, soma size, spine density, and dendritic intersections were made using FIJI/ImageJ. Solutions in mM. Cutting solution: 225 sucrose, 13.9 NaCl, 26.2 $NaHCO_3$, 1 NaH_2PO_4, 1.25 glucose, 2.5 KCl, 0.1 $CaCl_2$, 4.9 $MgCl_2$, 4.9 $MgCl_2$, and 3 kynurenic acid. ACSF: 124 NaCl, 2.5 KCl, 2.5 $CaCl_2$, 1.3 $MgCl_2$, 26.2 $NaHCO_3$, 1 NaH_2PO_4 and 20 glucose (310-320 mOsm). $KMeSO_4$ internal: 120 $KMeSO_4$, 20 KCl, 10 HEPES, 0.2 K-EGTA, 2 $MgCl_2$, 4 Na-ATP, and 0.4 Na-GTP (pH = 7.25, 290 mOsm).

Operant training: Mice were allowed to recover from surgery for 21-28 days prior to behavioral testing. One week prior to training, mice were gradually food restricted to 85-90% body weight. Mice were placed in modular chambers (Med Associates) with two

illuminated nose poke ports and a trough pellet receptacle. Mice were first trained on a fixed ratio 1 (FR1) schedule with one active and one inactive nose poke port. Active and inactive sides were counterbalanced across groups. Sessions lasted 30 min or until 50 pellets were earned, whichever occurred sooner. A rewarded nose poke triggered a pellet to be dispensed into the trough receptacle and a pure tone to play for 1 s. For the first 3 days of training, the pellet receptacle was baited with between one and three chocolate pellets (Bio-Serv, F05301) and both nose poke ports were baited with dust from crushed chocolate pellet. Mice were run on FR1 schedule until criteria, at which point they were moved to FR3. The criterion for phase completion was 3 consecutive days with at least 30 earned rewards and 75% discrimination of the active lever. After reaching criteria at FR3, mice were tested in a 1-day progressive ratio task. The progressive ratio task was based on a protocol modified for mice by Johnson et al. (2022[35]), but with a maximum session time of 30 min. Mice were excluded if they failed to reach criteria after 10 days. Three mice were excluded from fiber photometry experiments due to non-responding. For CRF cKO studies, four mice (two control, two cKO) were excluded due to poor viral injection.

Fiber photometry: Mice were trained on an operant task as described above. During training, mice were attached to a 200µm core fiberoptic patchcord (Doric) by a black covered zirconia mating sleeve (Doric) to reduce light leakage. Mice were attached every day of training, but recordings were only performed on alternating days to prevent bleaching. A Doric/TDT fiber photometry system was used to record fluorescence. This system included: integrated fluorescence mini-cube (Doric), femtowatt photoreceiver module (Doric, 2151), LED driver (Doric, LEDD_2), two connectorized LEDs (Doric, CLED_405 and CLED_465), patch panel (Tucker Davis Technologies, PP24), fiber photometry processor (TDT, RZ5P) and high-performance computer workstation (TDT, WS4) with synapse software (TDT) to control the LEDs and collect data. A 10 Hz lowpass filter was applied at the time of collection, and LED outputs were calibrated daily to 40µW output at the patchcord tip. TTLs generated by Med-PC (Med Associates) were used to time-lock recordings with behavioral events (nose poke, entry into the magazine, reward dispensed). Analysis of photometry signals was done using the

Python toolbox GuPPy, created by the Lerner Lab[33]. A zero phase moving average linear digital filter was used with a 100 data point window. An isosbestic control channel (405 nm) was used to filter out artifacts, and a standard z-score was calculated. The Med-PC generated timestamps were used to align z-scores from behavioral events, and these z-scores were first averaged by session then by mouse.

Following fiber photometry recordings, mice were anesthetized with pentobarbital (Fatal-Plus; 100mg/kg, i.p.), and transcardially perfused with ice cold 1x PBS (8 mL) followed by 4% PFA (50 mL). Brains were post-fixed in 4% PFA for 24 hours, then sunk in 30% sucrose in 1x PBS for 48-72 hours. On a microtome (ThermoFisher Microm HM 450), tissue was sectioned in 40 μM coronal slices free floating in 1x PBS with 0.01% sodium azide. Sections containing NAc were mounted onto slides and fiber placement was confirmed by microscopy.

Sucrose preference: Mice were individually housed for the duration of sucrose preference testing. Each cage was given two identical water bottles, which were weighed every 24 hours (same time of day) and placed back into the opposite side of the cage after weighing. On days 1-4, both water bottles were filled with water in order to habituate the animals. On days 5-7, one of the two bottles contained 1% sucrose solution. The sucrose bottle side was counterbalanced across groups and switched daily after weighing. A dummy cage containing water/water on days 1-4 and sucrose/water on days 5-7 was also weighed to control for non-drinking loss of liquid and ensure that water and sucrose had comparable ambient loss. Sucrose preference was calculated for each mouse each day by calculating the percentage of daily intake that was sucrose [sucrose/(sucrose+water)].

Open field exploration**:** Open-field locomotion was measured in large custom made acrylic chambers (50 x 50x 40 cm) for 60 minutes using video monitoring and Noldus Ethovision software.

Quantitative polymerase chain reaction: The nucleus accumbens was rapidly dissected from *Crh*$^{loxP/loxP}$ mice transduced with AAV5-CMV-eGFP or AAV5-CMV-Cre-eGFP and

stored in the -20 freezer in RNAlater. Primers used for PCR of the *Crh*^{loxP} (*Crh*-Forward: TTTATGGCCTTCCTCGTTAG; *Crh*-Reverse: TCTGTCGTTACTATGGCCTG). Total RNA was purified using RNeasy Micro (Qiagen). RNA was quantified using a Nanodrop and cDNA was synthesized using an Invitrogen kit. qPCR for RNAs for *GAPDH* and *Crh* were run using TaqMan Gene Expression Assays (Thermofisher, Cat#4331182). We determined relative mRNA expression of the endogenous control gene GAPDH and *Crh*, respectively. Quantitative PCR (qPCR) was performed using TaqMan Fast Polymerase (Applied Biosystems) in a StepOnePlus Real-Time PCR system. Cycling conditions were as follows: initial hold at 95°C for 20 s; 40 cycles of step 1 (95°C for 1 s); and step 2 (60°C for 20 s). Samples were run in quadruplicate, and negative controls were run in parallel. cDNA synthesis and qPCR experiments were repeated three times. Relative quantification was calculated using the ΔΔCt method (StepOne System Software, Applied Biosystems).

Corticosterone ELISA: Mice were killed by rapid decapitation and trunk blood was collected. Trunk blood was allowed to coagulate for 30 min at room temperature. Samples were then centrifuged for 10 min at 2000 x g. Serum was collected and stored at -20°C. ELIZA was run according to manufacturer instructions (Enzo, ADI-900-097). In brief, samples were pipetted into the assay plate, then buffer, blue and yellow conjugates are added. The plate is incubated for 2 hrs with agitation (up to 500 rpm). Wells are then emptied and washed three times before pNpp substrate is added and incubated for 1 hr. Finally, stop solution is added and optical density measured on a microplate reader (SpectraMax, Molecular Devices). Corticosterone standards (20000, 4000, 800, 160, 32 pg/mL) were run alongside and used to fit a 4 parameter logistic curve.

References

1 Berridge, K. C. & Kringelbach, M. L. Neuroscience of affect: brain mechanisms of pleasure and displeasure. *Curr Opin Neurobiol* **23**, 294-303 (2013). https://doi.org:10.1016/j.conb.2013.01.017

2 Gruber, A. J., Hussain, R. J. & O'Donnell, P. The nucleus accumbens: a switchboard for goal-directed behaviors. *PLoS One* **4**, e5062 (2009). https://doi.org:10.1371/journal.pone.0005062

3 Castro, D. C. & Bruchas, M. R. A Motivational and Neuropeptidergic Hub: Anatomical and Functional Diversity within the Nucleus Accumbens Shell. *Neuron* **102**, 529-552 (2019). https://doi.org:10.1016/j.neuron.2019.03.003

4 Russo, S. J. & Nestler, E. J. The brain reward circuitry in mood disorders. *Nat Rev Neurosci* **14**, 609-625 (2013). https://doi.org:10.1038/nrn3381

5 Al-Muhtasib, N., Forcelli, P. A. & Vicini, S. Differential electrophysiological properties of D1 and D2 spiny projection neurons in the mouse nucleus accumbens core. *Physiol Rep* **6**, e13784 (2018). https://doi.org:10.14814/phy2.13784

6 Kravitz, A. V. *et al.* Regulation of parkinsonian motor behaviours by optogenetic control of basal ganglia circuitry. *Nature* **466**, 622-626 (2010). https://doi.org:10.1038/nature09159

7 Kravitz, A. V., Tye, L. D. & Kreitzer, A. C. Distinct roles for direct and indirect pathway striatal neurons in reinforcement. *Nat Neurosci* **15**, 816-818 (2012). https://doi.org:10.1038/nn.3100

8 Lobo, M. K. *et al.* Cell type-specific loss of BDNF signaling mimics optogenetic control of cocaine reward. *Science* **330**, 385-390 (2010). https://doi.org:10.1126/science.1188472

9 Gerfen, C. R. Segregation of D1 and D2 dopamine receptors in the striatal direct and indirect pathways: An historical perspective. *Front Synaptic Neurosci* **14**, 1002960 (2022). https://doi.org:10.3389/fnsyn.2022.1002960

10 Nakanishi, S., Hikida, T. & Yawata, S. Distinct dopaminergic control of the direct and indirect pathways in reward-based and avoidance learning behaviors. *Neuroscience* **282**, 49-59 (2014). https://doi.org:10.1016/j.neuroscience.2014.04.026

11 Chen, A. P. F., Chen, L., Kim, T. A. & Xiong, Q. Integrating the Roles of Midbrain Dopamine Circuits in Behavior and Neuropsychiatric Disease. *Biomedicines* **9** (2021). https://doi.org:10.3390/biomedicines9060647

12 Bamford, I. J. & Bamford, N. S. The Striatum's Role in Executing Rational and Irrational Economic Behaviors. *Neuroscientist* **25**, 475-490 (2019). https://doi.org:10.1177/1073858418824256

13 Chen, R. *et al.* Decoding molecular and cellular heterogeneity of mouse nucleus accumbens. *Nat Neurosci* **24**, 1757-1771 (2021). https://doi.org:10.1038/s41593-021-00938-x

14 Saunders, A. *et al.* Molecular Diversity and Specializations among the Cells of the Adult Mouse Brain. *Cell* **174**, 1015-1030 e1016 (2018). https://doi.org:10.1016/j.cell.2018.07.028

15 Gokce, O. *et al.* Cellular Taxonomy of the Mouse Striatum as Revealed by Single-Cell RNA-Seq. *Cell Rep* **16**, 1126-1137 (2016). https://doi.org:10.1016/j.celrep.2016.06.059
16 Merchenthaler, I., Vigh, S., Schally, A. V., Stumpf, W. E. & Arimura, A. Immunocytochemical localization of corticotropin releasing factor (CRF)-like immunoreactivity in the thalamus of the rat. *Brain Res* **323**, 119-122 (1984). https://doi.org:10.1016/0006-8993(84)90272-5
17 Baumgartner, H. M., Schulkin, J. & Berridge, K. C. Activating Corticotropin-Releasing Factor Systems in the Nucleus Accumbens, Amygdala, and Bed Nucleus of Stria Terminalis: Incentive Motivation or Aversive Motivation? *Biol Psychiatry* **89**, 1162-1175 (2021). https://doi.org:10.1016/j.biopsych.2021.01.007
18 Henckens, M. J., Deussing, J. M. & Chen, A. Region-specific roles of the corticotropin-releasing factor-urocortin system in stress. *Nat Rev Neurosci* **17**, 636-651 (2016). https://doi.org:10.1038/nrn.2016.94
19 Lemos, J. C. *et al.* Severe stress switches CRF action in the nucleus accumbens from appetitive to aversive. *Nature* **490**, 402-406 (2012). https://doi.org:10.1038/nature11436
20 Lim, M. M., Liu, Y., Ryabinin, A. E., Bai, Y., Wang, Z. & Young, L. J. CRF receptors in the nucleus accumbens modulate partner preference in prairie voles. *Hormones and behavior* **51**, 508-515 (2007).
21 Pecina, S., Schulkin, J. & Berridge, K. C. Nucleus accumbens corticotropin-releasing factor increases cue-triggered motivation for sucrose reward: paradoxical positive incentive effects in stress? *BMC biology* **4**, 8 (2006).
22 Refojo, D. *et al.* Glutamatergic and dopaminergic neurons mediate anxiogenic and anxiolytic effects of CRHR1. *Science* **333**, 1903-1907 (2011). https://doi.org:10.1126/science.1202107
23 Baumgartner, H. M., Granillo, M., Schulkin, J. & Berridge, K. C. Corticotropin releasing factor (CRF) systems: Promoting cocaine pursuit without distress via incentive motivation. *PLoS One* **17**, e0267345 (2022). https://doi.org:10.1371/journal.pone.0267345
24 Itoga, C. A. *et al.* New viral-genetic mapping uncovers an enrichment of corticotropin-releasing hormone-expressing neuronal inputs to the nucleus accumbens from stress-related brain regions. *J Comp Neurol* **527**, 2474-2487 (2019). https://doi.org:10.1002/cne.24676
25 Aschauer, D. F., Kreuz, S. & Rumpel, S. Analysis of transduction efficiency, tropism and axonal transport of AAV serotypes 1, 2, 5, 6, 8 and 9 in the mouse brain. *PLoS One* **8**, e76310 (2013). https://doi.org:10.1371/journal.pone.0076310
26 Assous, M., Faust, T. W., Assini, R., Shah, F., Sidibe, Y. & Tepper, J. M. Identification and Characterization of a Novel Spontaneously Active Bursty GABAergic Interneuron in the Mouse Striatum. *J Neurosci* **38**, 5688-5699 (2018). https://doi.org:10.1523/JNEUROSCI.3354-17.2018
27 Ibanez-Sandoval, O., Tecuapetla, F., Unal, B., Shah, F., Koos, T. & Tepper, J. M. A novel functionally distinct subtype of striatal neuropeptide Y interneuron. *J Neurosci* **31**, 16757-16769 (2011). https://doi.org:10.1523/JNEUROSCI.2628-11.2011

28 Tepper, J. M., Koos, T., Ibanez-Sandoval, O., Tecuapetla, F., Faust, T. W. & Assous, M. Heterogeneity and Diversity of Striatal GABAergic Interneurons: Update 2018. *Front Neuroanat* **12**, 91 (2018). https://doi.org:10.3389/fnana.2018.00091
29 Tepper, J. M., Tecuapetla, F., Koos, T. & Ibanez-Sandoval, O. Heterogeneity and diversity of striatal GABAergic interneurons. *Front Neuroanat* **4**, 150 (2010). https://doi.org:10.3389/fnana.2010.00150
30 Bengtsson Gonzales, C., Hunt, S., Munoz-Manchado, A. B., McBain, C. J. & Hjerling-Leffler, J. Intrinsic electrophysiological properties predict variability in morphology and connectivity among striatal Parvalbumin-expressing Pthlh-cells. *Sci Rep* **10**, 15680 (2020). https://doi.org:10.1038/s41598-020-72588-1
31 Gertler, T. S., Chan, C. S. & Surmeier, D. J. Dichotomous anatomical properties of adult striatal medium spiny neurons. *J Neurosci* **28**, 10814-10824 (2008). https://doi.org:10.1523/JNEUROSCI.2660-08.2008
32 Tepper, J. M., Sharpe, N. A., Koos, T. Z. & Trent, F. Postnatal development of the rat neostriatum: electrophysiological, light- and electron-microscopic studies. *Dev Neurosci* **20**, 125-145 (1998). https://doi.org:10.1159/000017308
33 Sherathiya, V. N., Schaid, M. D., Seiler, J. L., Lopez, G. C. & Lerner, T. N. GuPPy, a Python toolbox for the analysis of fiber photometry data. *Sci Rep* **11**, 24212 (2021). https://doi.org:10.1038/s41598-021-03626-9
34 Sanford, C. A. *et al.* A Central Amygdala CRF Circuit Facilitates Learning about Weak Threats. *Neuron* **93**, 164-178 (2017). https://doi.org:10.1016/j.neuron.2016.11.034
35 Johnson, A. R., Christensen, B. A., Kelly, S. J. & Calipari, E. S. The influence of reinforcement schedule on experience-dependent changes in motivation. *J Exp Anal Behav* **117**, 320-330 (2022). https://doi.org:10.1002/jeab.755
36 Holahan, M. R., Kalin, N. H. & Kelley, A. E. Microinfusion of corticotropin-releasing factor into the nucleus accumbens shell results in increased behavioral arousal and oral motor activity. *Psychopharmacology (Berl)* **130**, 189-196 (1997). https://doi.org:10.1007/s002130050228
37 Hikida, T. *et al.* Pathway-specific modulation of nucleus accumbens in reward and aversive behavior via selective transmitter receptors. *Proc Natl Acad Sci U S A* **110**, 342-347 (2013). https://doi.org:10.1073/pnas.1220358110
38 Yawata, S., Yamaguchi, T., Danjo, T., Hikida, T. & Nakanishi, S. Pathway-specific control of reward learning and its flexibility via selective dopamine receptors in the nucleus accumbens. *Proc Natl Acad Sci U S A* **109**, 12764-12769 (2012). https://doi.org:10.1073/pnas.1210797109
39 Silberman, Y., Matthews, R. T. & Winder, D. G. A corticotropin releasing factor pathway for ethanol regulation of the ventral tegmental area in the bed nucleus of the stria terminalis. *J Neurosci* **33**, 950-960 (2013). https://doi.org:10.1523/JNEUROSCI.2949-12.2013
40 Lemos, J. C., Shin, J. H. & Alvarez, V. A. Striatal cholinergic interneurons are a novel target of corticotropin releasing factor. *J Neurosci* (2019). https://doi.org:10.1523/JNEUROSCI.0479-19.2019

41 Maniam, J. & Morris, M. J. The link between stress and feeding behaviour. *Neuropharmacology* **63**, 97-110 (2012). https://doi.org:10.1016/j.neuropharm.2012.04.017
42 Beninger, R. J. & Miller, R. Dopamine D1-like receptors and reward-related incentive learning. *Neurosci Biobehav Rev* **22**, 335-345 (1998). https://doi.org:10.1016/s0149-7634(97)00019-5
43 Deussing, J. M. & Chen, A. The Corticotropin-Releasing Factor Family: Physiology of the Stress Response. *Physiological Reviews* **98**, 2225-2286 (2018). https://doi.org:10.1152/physrev.00042.2017
44 Bryce, C. A. & Floresco, S. B. Alterations in effort-related decision-making induced by stimulation of dopamine D(1), D(2), D(3), and corticotropin-releasing factor receptors in nucleus accumbens subregions. *Psychopharmacology (Berl)* **236**, 2699-2712 (2019). https://doi.org:10.1007/s00213-019-05244-w
45 Hupalo, S., Bryce, C. A., Bangasser, D. A., Berridge, C. W., Valentino, R. J. & Floresco, S. B. Corticotropin-Releasing Factor (CRF) circuit modulation of cognition and motivation. *Neurosci Biobehav Rev* **103**, 50-59 (2019). https://doi.org:10.1016/j.neubiorev.2019.06.010
46 Faul, F., Erdfelder, E., Buchner, A. & Lang, A. G. Statistical power analyses using G*Power 3.1: tests for correlation and regression analyses. *Behav Res Methods* **41**, 1149-1160 (2009). https://doi.org:10.3758/BRM.41.4.1149
47 Faul, F., Erdfelder, E., Lang, A. G. & Buchner, A. G*Power 3: a flexible statistical power analysis program for the social, behavioral, and biomedical sciences. *Behav Res Methods* **39**, 175-191 (2007). https://doi.org:10.3758/bf03193146
48 Beier, K. T. *et al.* Circuit Architecture of VTA Dopamine Neurons Revealed by Systematic Input-Output Mapping. *Cell* **162**, 622-634 (2015). https://doi.org:10.1016/j.cell.2015.07.015
49 Chen, T. W. *et al.* Ultrasensitive fluorescent proteins for imaging neuronal activity. *Nature* **499**, 295-300 (2013). https://doi.org:10.1038/nature12354

Figure 1. Characterization of NAc CRF neurons using fluorescent in situ hybridization

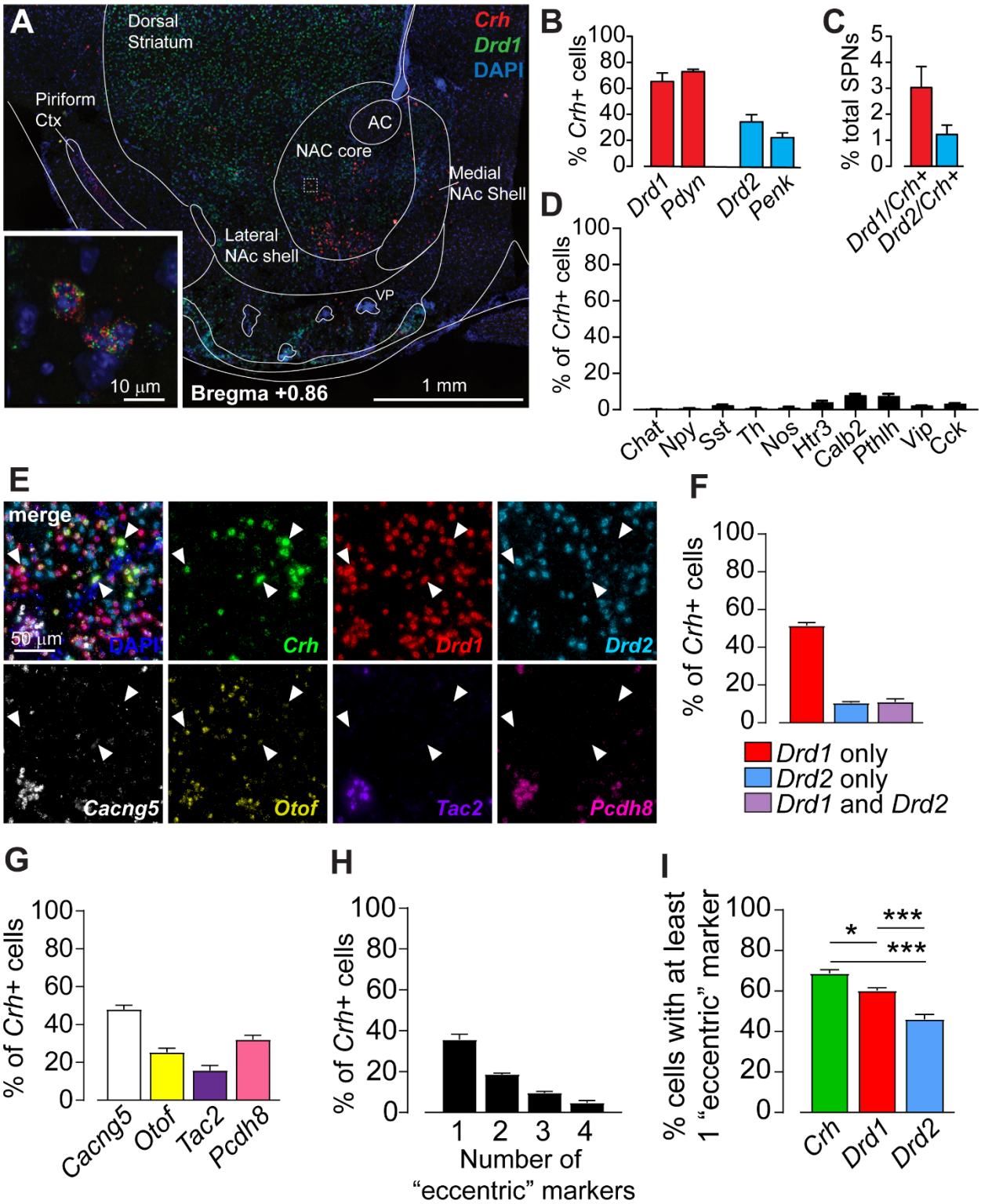

Figure 1. Characterization of NAc CRF neurons using fluorescent in situ hybridization: (A) Representative image of fluorescent in situ hybridization expression in NAc and co-expression of *Crh* (red) and *Drd1* (green) mRNA counterstained with DAPI (blue). (B) Quantification of co-localization of *Drd1* (N = 12), *Pdyn* (N = 3), *Drd2* (N = 11), and *Penk* (N = 3) mRNA transcripts in *Crh*-expressing cells. (C) Proportion of *Drd1* (N = 12) and *Drd2* (N = 11) populations expressing *Crh* mRNA. (D) mRNA expression of interneuron markers in *Crh*+ cells: *Chat* (N = 4)*, Npy* (N = 10)*, Sst* (N = 10)*, Th* (N = 4)*, Nos* (N = 4)*, Htr3* (N = 6)*, Calb2* (N = 8)*, Pthlh* (N = 7)*, Vip* (N = 5)*,* and *Cck* (N = 7) (E) Representative images from the HiPlex assay, demonstrating fluorescent labeling of seven distinct mRNA transcripts in the same tissue, counterstained with DAPI. To characterize the *Crh*+ population, probes for *Crh*, canonical SPN markers (*Drd1*: red; *Drd2*: blue), and "eccentric" SPN markers (*Cacng5*: white; *Otof*: yellow; *Tac2*: purple; *Pcdh8*: pink) were simultaneously visualized in NAc. (F) Quantification of the HiPlex assay for *Drd1* only*, Drd2* only or *Drd1/Drd2* co-expressing cells within the *Crh* population (N = 8). (G) Analysis of co-localization of "eccentric" markers (*Cacng5, Otof, Tac2,* and *Pcdh8*) with *Crh* mRNA (N = 8). (H) Distribution of *Crh* cells expressing either one, two, three or all four eccentric markers assayed (I) Comparison of the proportion of *Crh, Drd1,* or *Drd2* cells expressing at least one "eccentric" marker. The *Crh* population had a significantly higher proportion of cells expressing at least one "eccentric" marker compared to *Drd1* and *Drd2* populations. Additionally, a higher proportion of *Drd1* cells expressed "eccentric" markers compared to *Drd2* cells (one-way ANOVA with Sidak post-hoc, *p = 0.0114, ***p < 0.0001; N = 8). (Data are represented as mean ± SEM. All N represent the number of animals used).

Figure 2. NAc CRF neurons project to ventral pallidal and midbrain regions

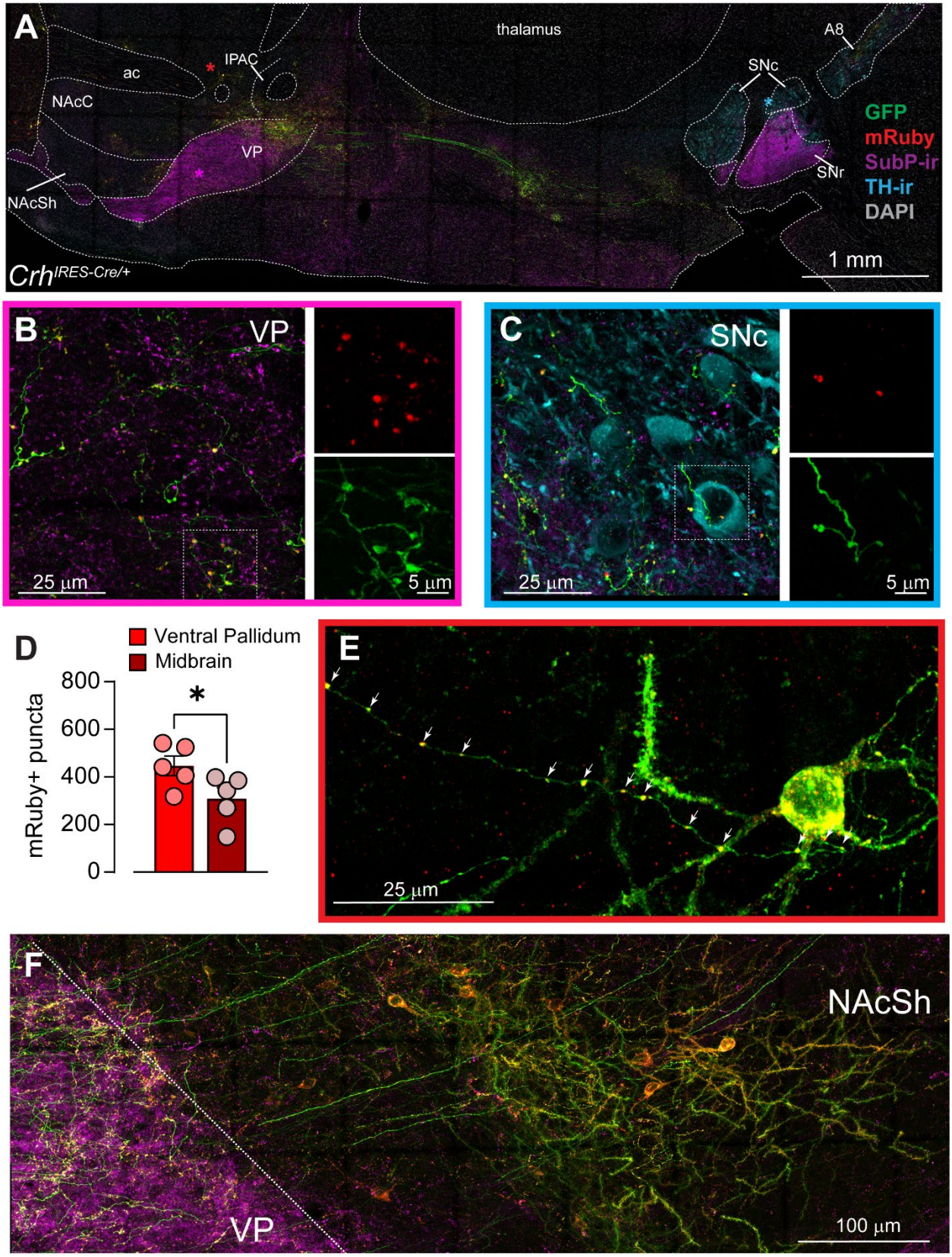

Figure 2. NAc CRF neurons project to ventral pallidal and midbrain regions (A-C) Representative image of a sagittal section from a *Crh*$^{IRES\text{-}Cre/-}$ mouse injected with AAV5-hSyn-FLEX-GFP-Synaptophysin-mRuby into the NAc. Sections were processed for Substance P (SubP, magenta) and tyrosine hydroxylase (TH, cyan) immunoreactivity. GFP+ (green) fibers can be seen along projections, with mRuby+ (red) terminals in (B) ventral pallidum and (C) midbrain. (D) Quantification of mRuby+ puncta in ventral pallidum and midbrain. Significantly more puncta were found in the ventral pallidum, suggesting this is the main projection target of NAc CRF cells (paired t-test, $p = 0.0165$; N = 5 animals, 3 sections each). (E) High resolution image of a virally transfected putative CRF cell. mRuby+ varicosities (white arrows) can be seen along the GFP+ fiber. (F) Example image of an accumbal CRF cell cluster near the boundary between NAc and ventral pallidum (delineated by SubP). (Data are represented as mean ± SEM) (ac: anterior commissure, IPAC: posterior limb of the anterior commissure, NAcC: nucleus accumbens core, NAcSh: nucleus accumbens shell, SNc: substantia nigra *pars compacta*, SNr: substantia nigra *pars reticulata*, VP: ventral pallidum)

Figure 3. Electrophysiological examination NAc CRF+ neurons reveals three subtypes

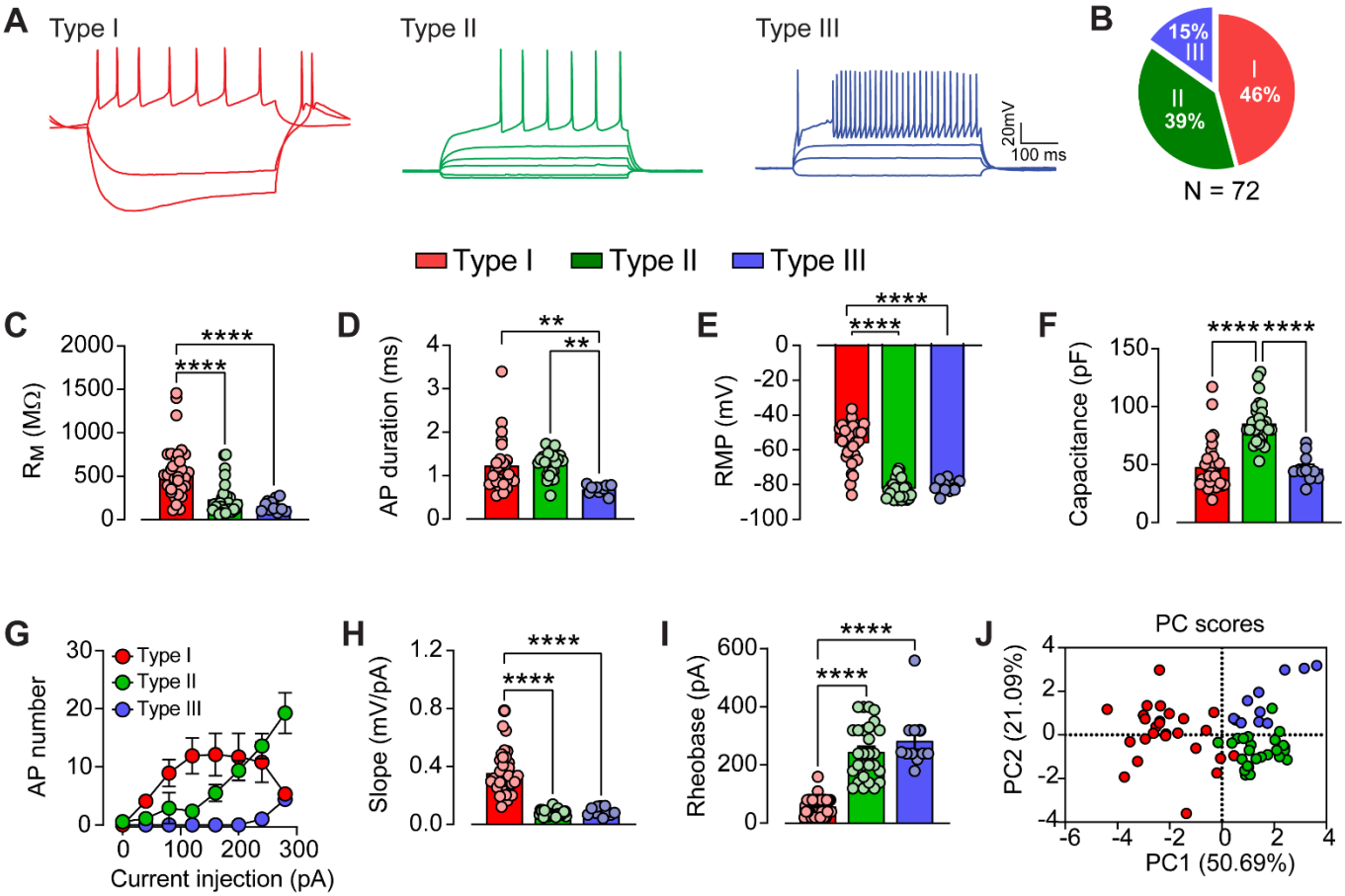

Figure 3. Electrophysiological examination of NAc CRF+ neurons reveals three subtypes (A) Representative electrophysiological traces of firing patterns of CRF cell subtypes 1, 2 and 3 in response to current injections (-120 to +360, 40pA steps). (B) Proportion of NAc CRF cells that are Type 1 (red; N_{cells} = 33), Type 2 (green; N_{cells} = 28) or Type 3 (blue; N_{cells} = 11). (C) Membrane resistance (R_M) of CRF cell subtypes. Type 1 cells had significantly higher membrane resistance compared to Type 2 and Type 3 cells. (D) Average action potential (AP) duration across CRF cell subtypes. Type 3 cells had a significantly shorter AP duration compared to Type 1 and Type 2 cells. (E) Resting membrane potential (RMP) across CRF cell subtypes. Type 1 cells had a significantly higher resting potential compared to Type 2 and Type 3 cells. Type 2 and Type 3 cells were indistinguishable in this measure. (F) Membrane capacitance across CRF cell subtypes. Type 2 cells had significantly higher capacitance compared to Type 1 and Type 3 cells. (E) Firing-current curves (F-I curves) of Type 1, Type 2 and Type 3 cells, showing distinct F-I relationships. (H) Subthreshold IV slope of CRF+ cell subtypes. Type 1 cells had a significantly higher slope than Type 2 and Type 3 cells. (I) Rheobase of CRF cell subtypes. Type 1 cells had a significantly lower rheobase compared to Type 2 and Type 3 cells. (J) Unsupervised principal component analysis of all NAc CRF neurons. Each cell is colored with their experimenter-determined subtype. The three subtypes could be visualized along two PCs, with some overlap between groups. (Data are represented as mean ± SEM) (**$p < 0.01$, ****$p < 0.0001$, post-hoc-tests following one-way ANOVA.)

Figure 4. Accumbal CRF subtype confers discrete morphological profile

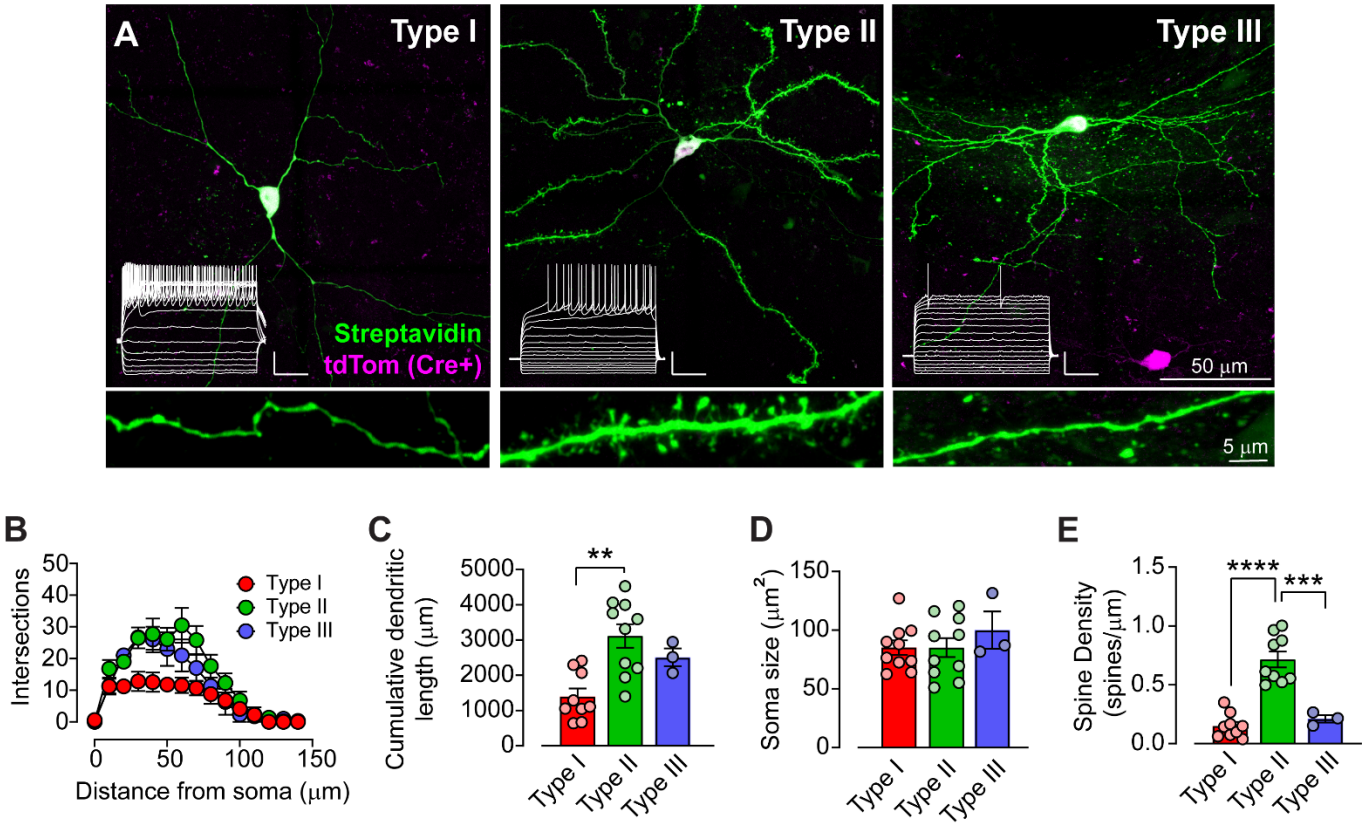

Figure 4. Accumbal CRF subtype confers discrete morphological profile (A) Example images of CRF neuron subtypes from *Crh*$^{IRES\text{-}Cre/-}$; Ai14 mice used for recordings and morphological analysis. tdTomato (pink) expression driven by Cre recombination was used to identify CRF+ cells which were filled with biocytin during recording, and post-hoc stained for streptavidin (green). (inset) Example traces from pictured cells in response to a step-current protocol. (B) Sholl analysis of dendritic intersections as a function of distance from soma across CRF cell subtypes. Type 1 (red; N_{cells} = 9) cells had significantly fewer intersections compared to Type 2 (green; N_{cells} = 10) and Type 3 (blue; N_{cells} = 3) cells. (C) Analysis of the total dendritic length across CRF cell subtypes. Type 1 had significantly smaller cumulative dendritic length compared to Type 2 or Type 3 cells. (D) Comparison of soma size between CRF cell subtypes, with no significant difference between groups. (E) Quantification of dendritic spine density across subtypes of CRF cells. Type 2 cells had significantly increased spine density compared to Type 1 and Type 3 cells. (Data are represented as mean ± SEM; scale bar: 25mV, 100ms) (**p = 0.0010, ***p = 0.0003, **** p < 0.0001, one-way ANOVA.)

Figure 5. Juvenile Drd1+ cells have a blended electrophysiological profile

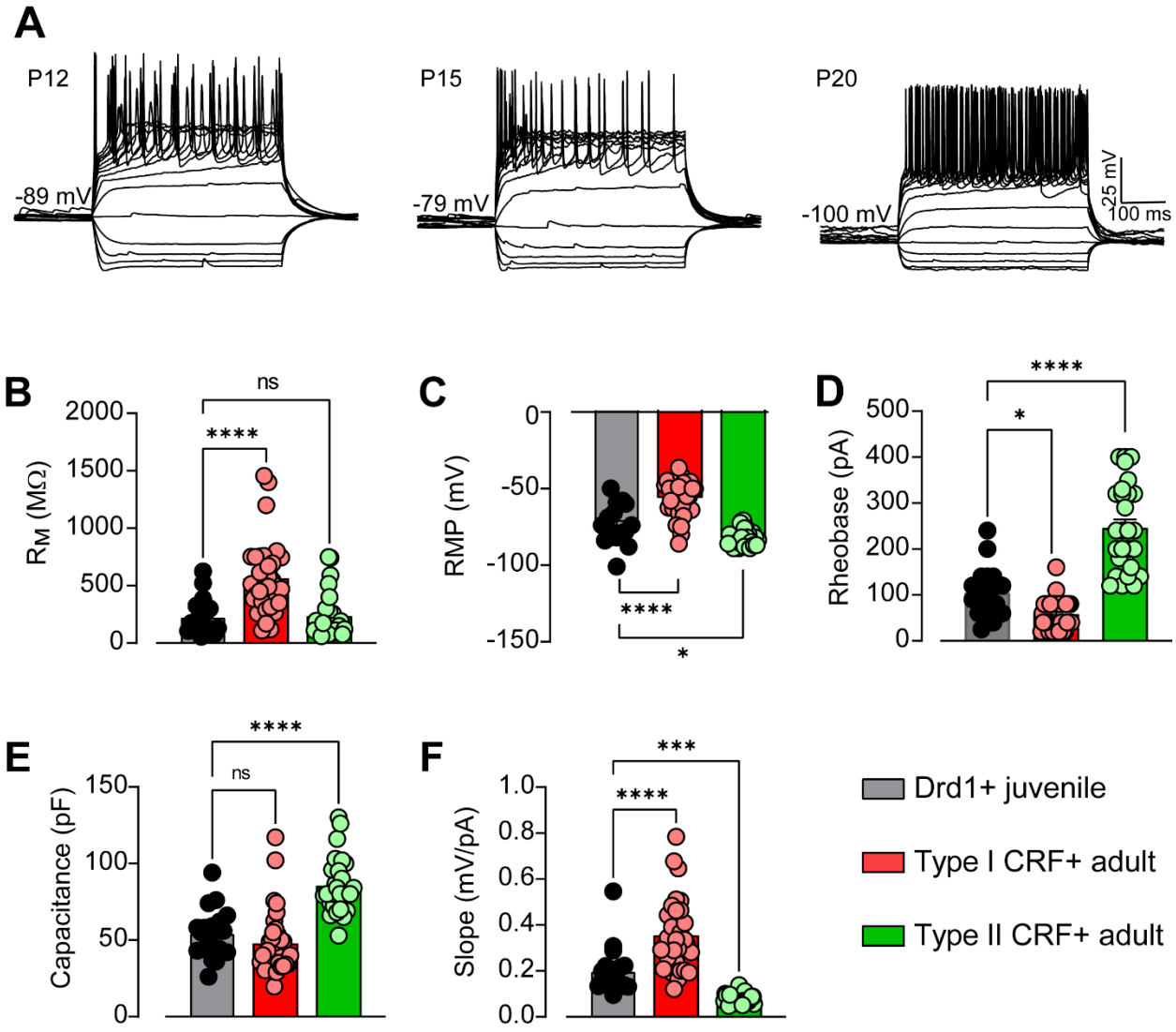

Figure 5. Juvenile Drd1+ cells have a blended electrophysiological profile (A) Example traces from Drd1+ neurons recorded *Drd1*^{tdTomato} mice of firing patterns in response to a step-current protocol at postnatal day 12, 15 and 20. (B) Membrane resistance in juvenile Drd1+ cells (grey) and adult CRF+ Type 1 (red) or Type 2 (green) cells. Juvenile Drd1+ cells had significantly lower membrane resistance than adult Type 1 cells, but there was no difference between juvenile Drd1+ cells and adult Type 2 cells. (C) Resting membrane potential (RMP) in juvenile Drd1+ cells, adult Type I CRF+ cells, and adult Type 2 CRF+ cells. Juvenile Drd1+ cells had an intermediate phenotype, with their RMP being significantly lower than adult Type 1 cells and significantly higher than adult Type 2 cells. (D) Rheobase of juvenile Drd1+ cells, adult CRF+ Type 1 and Type 2 cells. Similar to RMP, rheobase for juvenile Drd1+ cells was between that of adult Type 1 and Type 2 CRF+ populations. The juvenile Drd1+ rheobase was significantly higher than that of Type 1 cells, but lower than adult Type 2 cells. (E) Capacitance of juvenile Drd1+, adult Type 1 CRF+, and adult Type 2 CRF+ cells. The juvenile Drd1+ cell capacitance was significantly lower than adult Type 2 cells, but not significantly different from that of adult Type 1 cells. (F) The subthreshold IV slope from juvenile Drd1+, adult Type 1 CRF+, and adult Type 2 CRF+ cells. Juvenile Drd1+ cells had an intermediate phenotype, with a slope significantly lower than adult Type 1 cells but significantly higher than the slope of adult Type 2 cells. (Data are represented as mean ± SEM) ($^{ns}p > 0.05$, $^{*}p < 0.05$, $^{***}p < 0.001$, $^{****}p < 0.0001$, Dunnett's post-hoc t-tests following one-way ANOVA.)

Figure 6. Activity patterns of NAc CRF cells are modulated in vivo by outcome of reward retrieval behavior

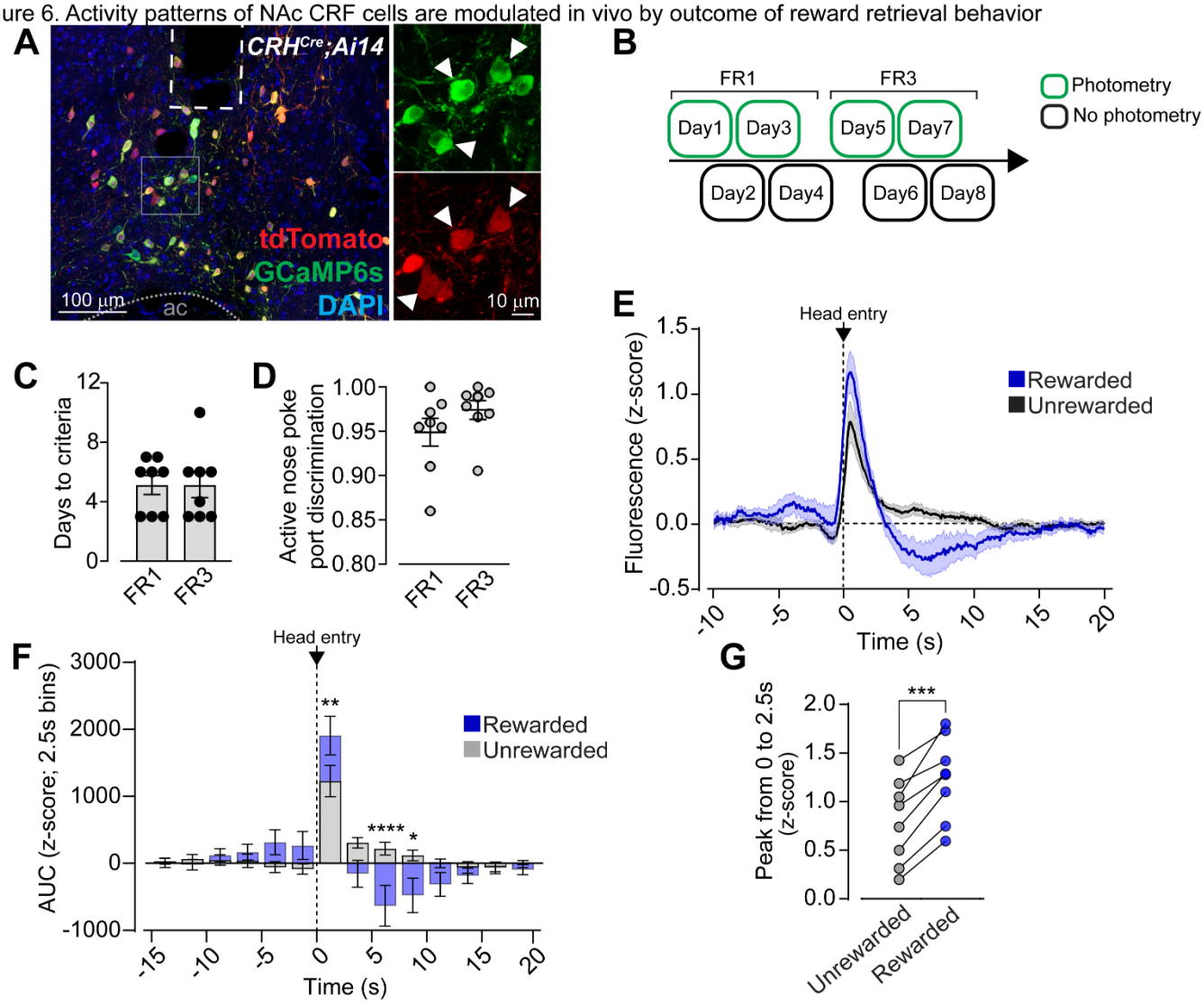

Figure 6. Activity patterns of NAc CRF cells are modulated in vivo by the outcome of reward retrieval behavior (A) Representative image of GCaMP6s (green) expression below the fiber optic tip (dotted line) in the NAc of *Crh*$^{IRES\text{-}Cre/-}$;Ai14 mice injected with AAV5-Syn-FLEX-GCaMP6s. Endogenous, Cre-driven tdTomato expression (red) can be seen co-localized with GCaMP6s viral particles (green), indicating recordings were of putative CRF+ cells (inset, white arrows). Counterstained with DAPI (blue). (B) Schematic of operant behavior task training and recording schedule. Mice were trained to a fixed ratio 1 (FR1) criteria, then fixed ratio 3 (FR3) criteria. Fiber photometry recordings were performed every other day. (C) Number of training days required for mice to reach criteria on FR1 and FR3 schedules. (D) Average discrimination of the active versus inactive nose poke ports across all FR1 and FR3 training days. (E) Average fluorescence (z-score) from NAc CRF cells time-locked to head entry into the reward magazine (t=0). Head entries were separated into those immediately following reward delivery when reward was present in the magazine (rewarded; blue) and head entries without reward delivery (unrewarded; black). (F) Area under the curve (AUC) for GCaMP6s fluorescence z-score binned into 2.5 s increments, time-locked to head entry into reward magazine. Rewarded head entries (blue) were accompanied by significantly higher fluorescence than unrewarded entries (grey) immediately following magazine entry, followed by significantly lower fluorescence 5–10 s after magazine entry (two-way ANOVA). (G) Within-subject comparison of the average peak fluorescence immediately following magazine head entry (0 to 2.5 s after entry) for each mouse. Rewarded head entries elicited significantly greater peak calcium responses compared to unrewarded head entries for every mouse (paired t-test). (Data are represented as mean ± SEM) (*$p < 0.05$, **$p < 0.01$, ***$p < 0.001$, **** $p < 0.0001$; N = 8)

Figure 7. Conditional knockdown of CRF from NAc promotes acquisition of rewarding action-outcome behavior

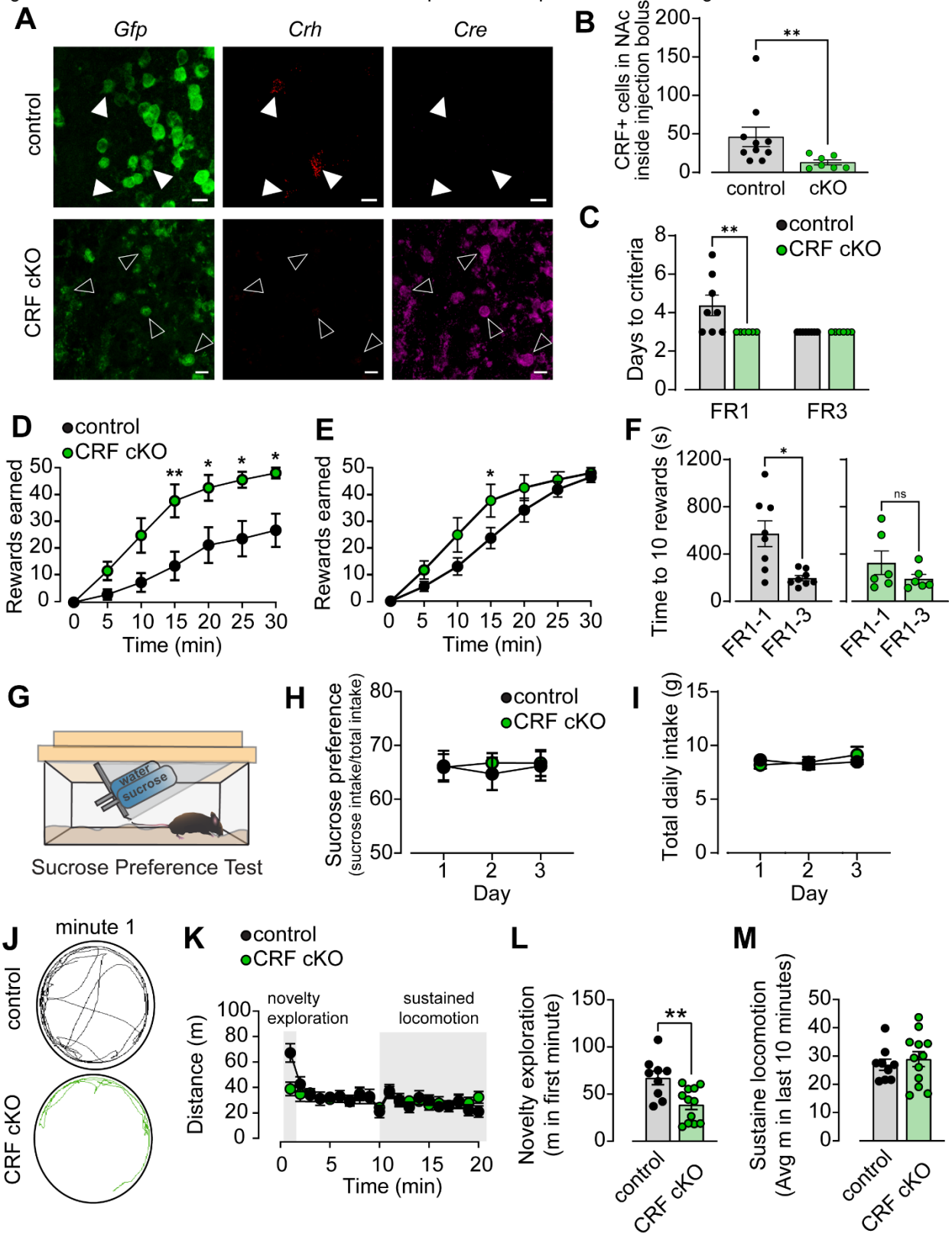

Figure 7. Conditional knockdown of CRF from NAc promotes acquisition of rewarding action-outcome behavior (A) Representative images from control (top) and CRF conditional knockout (bottom) mice. Either AAV8-CMV-eGFP (control) or AAV8-CMV-eGFP-Cre (CRF cKO) virus was bilaterally injected into the NAc of *Crh*$^{loxP/loxP}$ mice. Injections were validated by in situ hybridization for *Gfp* (green), *Crh* (red), and *Cre* (magenta) mRNA. In control mice, there was co-localization between *Gfp* and *Crh* (closed arrows), while CRF cKO animals had co-localization between *Gfp* and *Cre* (open arrows), but diminished co-localized of *Crh*. (B) Quantification of NAc CRF+ cells within the injection bolus of control (gray) or CRF cKO (green) mice. There was a significant reduction in the number of *Crh*+ cells in cKO mice (Mann-Whitney). (C) Days of testing required to reach criteria in an operant task with FR1 or FR3 reward schedule in control and CRF cKO mice. CRF cKO mice were significantly quicker to reach criteria in FR1 training. (D) Number of rewards earned over time on the first unbaited day of FR1 training and (E) on the first FR1 day in which criteria was reached. CRF cKO mice were significantly quicker to acquire rewards compared to controls. (F) Average time to earn 10 rewards in FR1 training on the first day (FR1-1) and third day (FR1-3) daily criteria was met. Control mice (grey, left) significantly reduced their time to 10 rewards across training, earning rewards faster on the third day. CRF cKO mice (green, right) did not show a difference in time to acquire 10 rewards between FR1 training days (paired t-test). (G) Schematic of sucrose preference test. (H) Sucrose preference in control (black, N = 8) and CRF cKO (green, N = 13) mice across 3 days of testing. There was no significant difference between groups. (I) Total daily liquid intake for control and CRF cKO mice over 3 days of sucrose preference testing. (J) Representative locomotion traces from control and CRF cKO mice during the first minute in a novel open field test. (K) Distance traveled by control and CRF cKO mice in the novel open field test, binned by 1 min increments. (L) Total distance traveled by control and CRF cKO mice during the “novelty exploration” phase of the novel open field test (defined as the first minute). Control mice traveled significantly more than CRF cKO mice during this first minute (unpaired t-test). (M) Average distance traveled by control and CRF cKO mice during the novel open field “sustained locomotion” period (defined as the last 10 m of the test). During this period, there were no significant locomotor differences between control and CRF cKO mice

(unpaired t-test). (Data are represented as mean ± SEM. Scale bar = 10 μm) ($^{ns}p > 0.05$, $^{*}p < 0.05$, $^{**}p < 0.01$, two-way repeated measures ANOVA with Sidak's post-hoc unless otherwise noted above.)

Supplemental Information for Eckenwiler et al.

Figure S1. Crh mRNA expression pattern in striatum

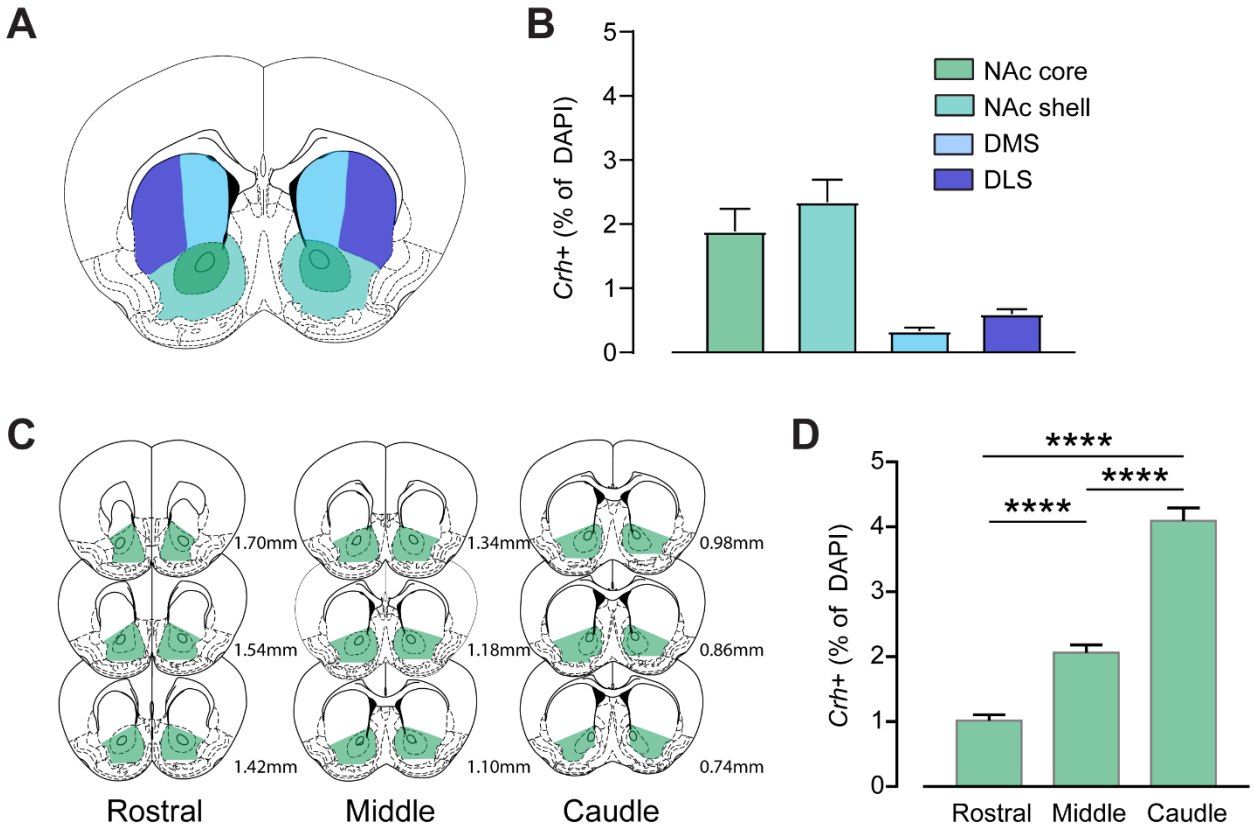

Figure S1, related to Figure 1. Crh mRNA expression pattern in striatum (A) Schematic of compartmentalization of dorsal medial striatum (DMS, light blue), dorsal lateral striatum (DLS, dark blue), nucleus accumbens core (NAc core, dark green), and nucleus accumbens shell (NAc shell, light green). (B) Quantification of in situ hybridization for *Crh* mRNA as percent of total DAPI+ cells in striatal compartments. *Crh*+ cells were more abundant in the NAc (NAc core: 2.42 ± 0.25%; NAc shell: 2.58 ± 0.27%) than in the dorsal striatum (DMS: 0.47 ± 0.05%; DLS: 0.61 ± 0.06%) (unpaired t-test, $p = 0.0135$; N = 6). (C) Schematic of rostral, medial and caudal delineations relative to bregma for NAc sections. (D) *Crh* mRNA expression as percent of total DAPI+ cells in NAc across the rostral-caudal axis. For analysis purposes, NAc was subregioned into rostral, middle and caudal compartments. NAc *Crh*+ expression followed a rostral to caudal gradient pattern. Rostral NAc contained the fewest Crh+ cells. Middle NAc contained significantly more than rostral NAc. Crh was the most abundant in caudal NAc compared to both rostral and middle compartments (Rostral: 1.013 ± 0.091%; Middle: 2.061 ± 0.121%; Caudal: 4.092 ± 0.198%; one-way ANOVA with Tukey: $F_{2,140} = 99.40$, $p < 0.0001$). (Data are represented as mean ± SEM.) (****$p < 0.0001$)

Figure S2. Validation of *Crh*$^{IRES\text{-}Cre/-}$ mouse line

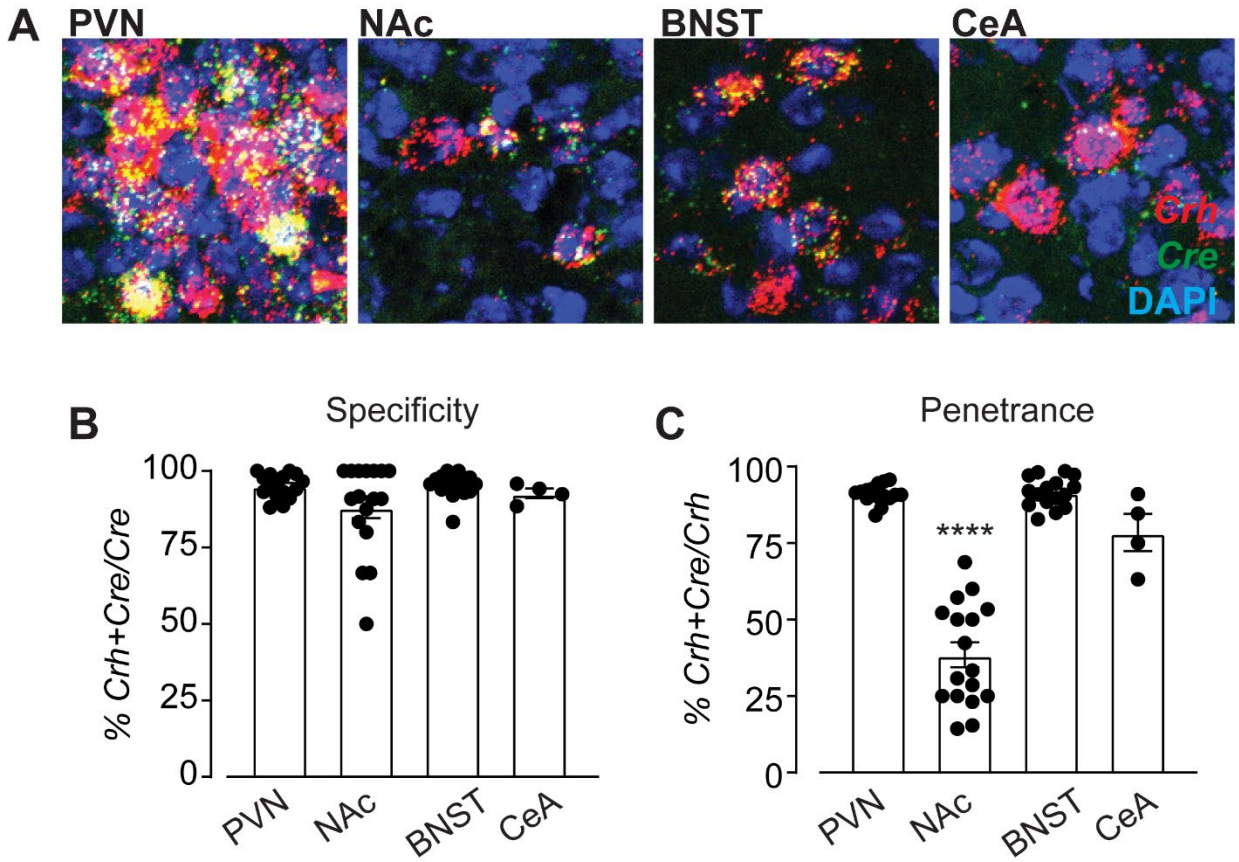

Figure S2, related to Figure 2. Validation of CRH$^{IRES\text{-}Cre/-}$ mouse line (A) Representative images of in situ hybridization expression from paraventricular nucleus of the hypothalamus (PVN), nucleus accumbens (NAc), bed nucleus of the stria terminalis (BNST) and central amygdala (CeA) from *Crh*$^{IRES\text{-}Cre/-}$ animals for *Crh* (red) and *Cre* (green) mRNA with DAPI counterstaining. (B) Specificity of the *Crh*$^{IRES\text{-}Cre/-}$ mouse line was assessed across regions as the percentage of *Cre*+ cells that were also positive for *Crh* RNA. There were no significant differences, with high specificity in all regions (PVN: 95 ± 1%; NAc: 88 ± 4%; BNST 93 ± 2%; CeA 95 ± 4%; one-way ANOVA: $F_{3,49} = 2.276$, $p = 0.09$, N = 4-16). (C) Penetrance of the *Crh*$^{IRES\text{-}Cre/-}$ mouse was assessed across regions as the percentage of *Crh*+ cells that were also positive for *Cre* RNA. Penetrance was high in the PVN, BNST and CeA, but was significantly reduced in the NAc (PVN: 91 ± 1%; NAc: 38 ± 4%; BNST 92 ± 1%; CeA 78 ± 6%; one-way ANOVA with Tukey: $F_{3,49} = 93.75$, $p < 0.0001$, N = 4-17). (Data are represented as mean ± SEM.) (****$p < 0.0001$)

Figure S3. *Crh*$^{IRES\text{-}Cre/-}$; Ai14 reporter expression and distribution of NAc CRF neuron subtypes

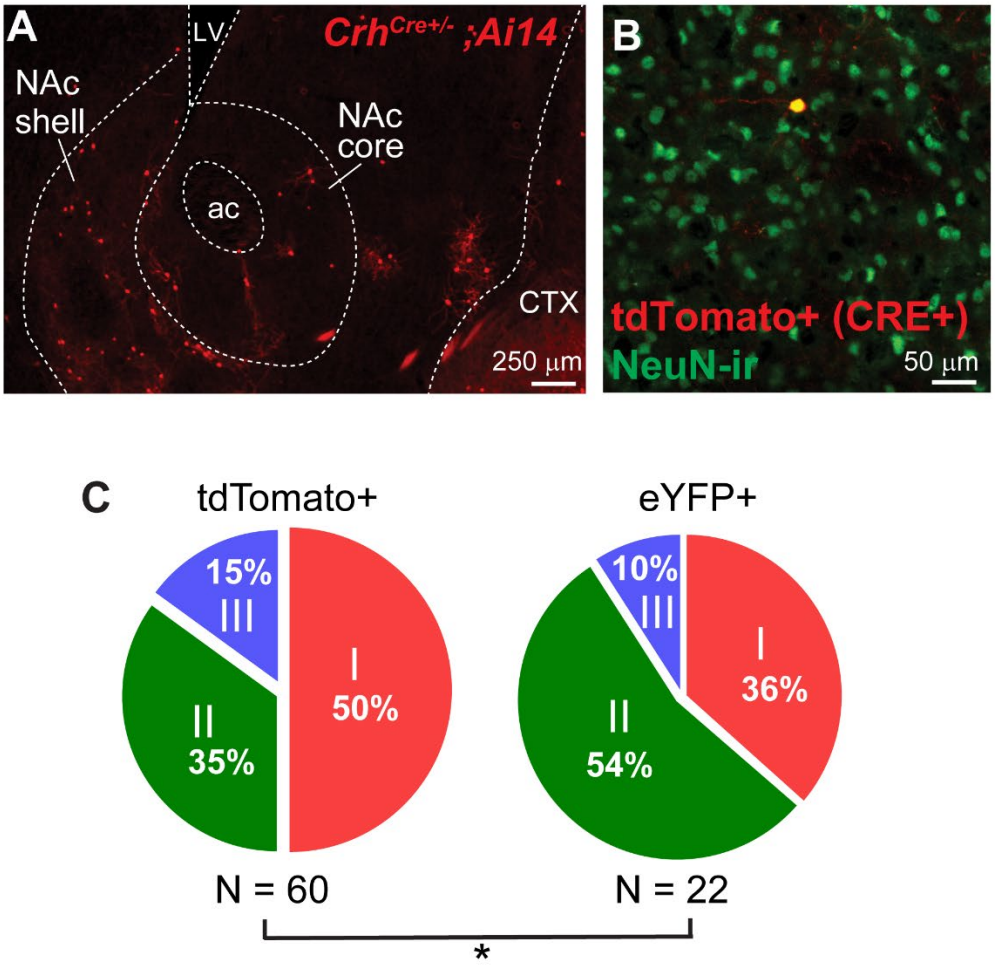

Figure S3, related to Figure 3. Crh*$^{IRES\text{-}Cre/-}$*; Ai14 reporter expression and proportions of NAc CRF neuron subtypes (A) Representative image from *Crh*$^{IRES\text{-}Cre/-}$; Ai14 reporter mouse of Cre-dependent tdTomato (red) expression in NAc. (B) High magnification image from *Crh*$^{IRES\text{-}Cre/-}$; Ai14 mouse with Cre-driven tdTomato (red) expression co-localized with a NeuN (green) positive cell body. (C) Relative proportions of subtypes from all NAc CRF+ neurons recorded from either *Crh*$^{IRES\text{-}Cre/-}$; Ai14 reporters (tdTomato+; left) or *Crh*$^{IRES\text{-}Cre/-}$ mice injected with AAV-DIO-eYFP viral particles (eYFP+; right). There was a shift in the distribution of CRF subtypes depending on which method was used, suggesting that there may be a developmental shift in the NAc CRF+ population (Chi-squared test, $p = 0.0255$).

Figure S4. Unsupervised clustering of NAc CRF cells based on electrophysiological properties

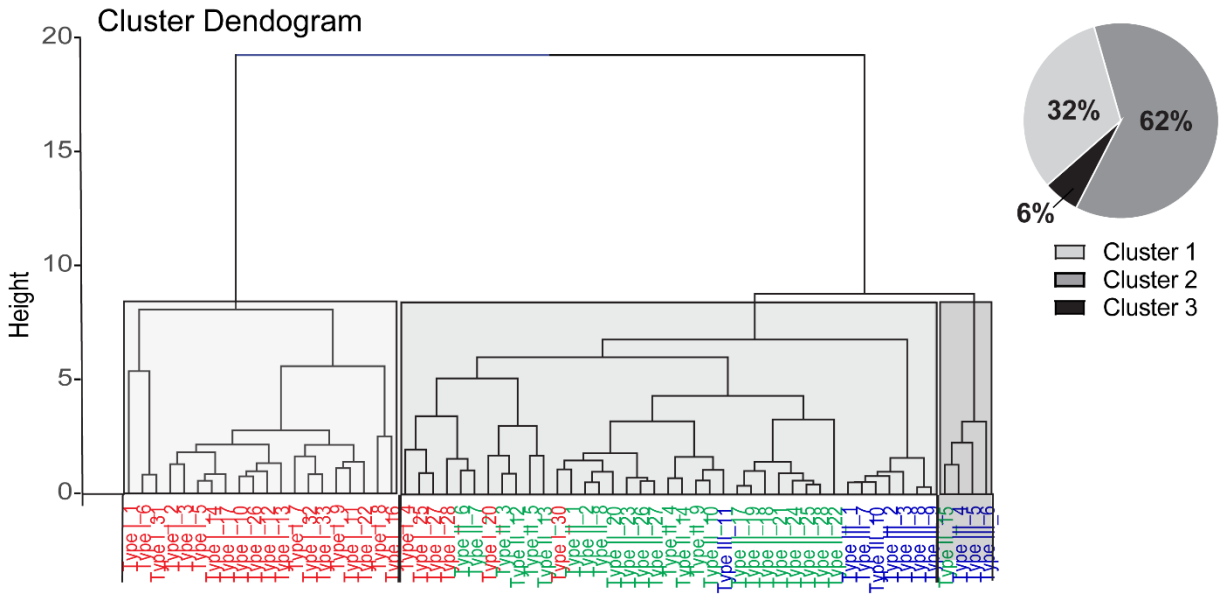

Figure S4, related to Figure 3. Unsupervised clustering of NAc CRF cells based on electrophysiological properties Hierarchical clustering of CRF cells based on active and passive electrophysiological components. While three clusters were sorted using this method, the experimenter defined subtypes (Type 1, red; Type 2, green; Type 3, blue) were not precisely replicated. The largest cluster, Cluster 2 (62%) is mostly comprised of Type 2 neurons but also contains a number of Type 1 and Type 3 cells. On the other hand, Cluster 1 (32%) is made up entirely of Type 1 neurons, while Cluster 3 (6%) is comprised of Type 3 cells with one exception.

Figure S5. NAc CRF neuronal activity patterns during early verses late fixed-ratio (FR1) training

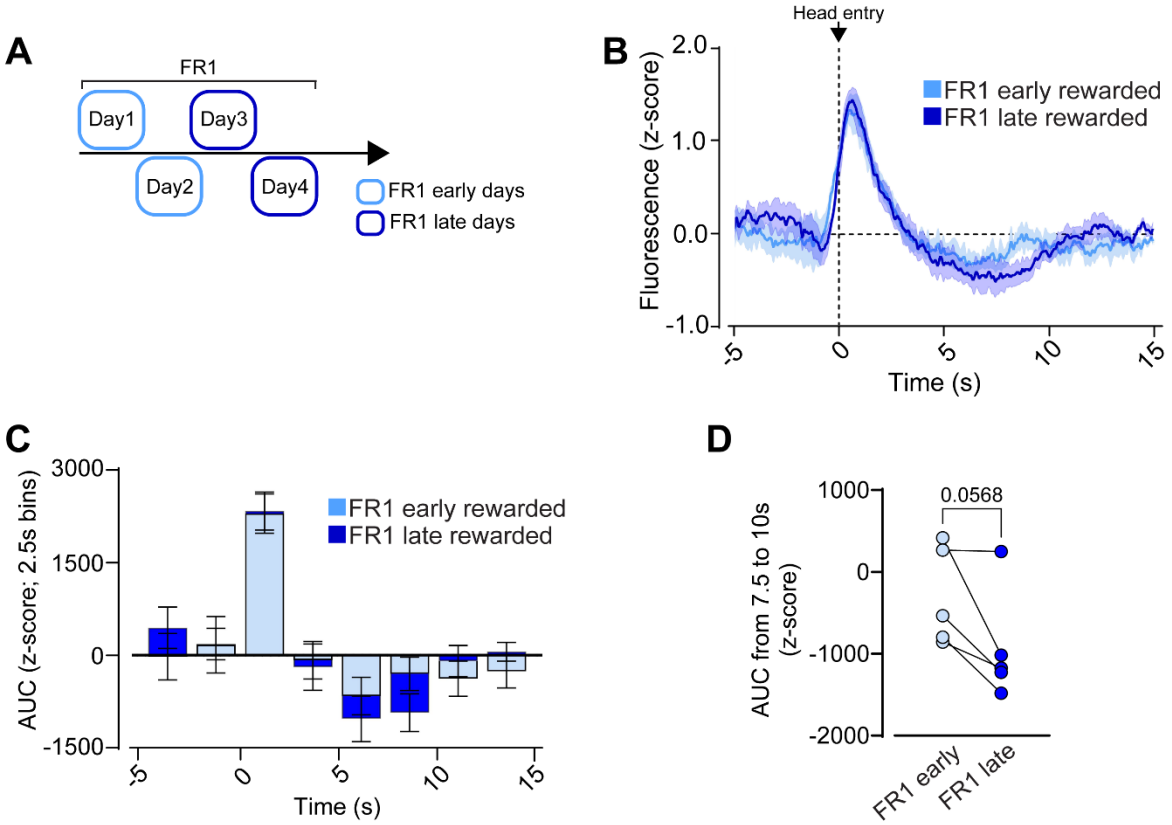

Figure S5, related to Figure 6. NAc CRF neuronal activity patterns during early verses late fixed-ratio (FR1) training (A) Schematic detailing delineation of 'early FR1' and 'late FR1' days for the purpose of analysis. (B) Average fluorescence (z-score) of NAc CRF neurons time-locked to successful (rewarded) magazine head entry (at t = 0) in early and late phase FR1 training. GCaMP6s fluorescence recorded with fiber photometry performed in *Crh*$^{IRES\text{-}Cre/-}$ mice with optic fiber implant and viral injection (AAV5-Syn-FLEX-GCaMP6s) into NAc. (C) Area under the curve (AUC) of GCaMP6s fluorescence relative to rewarded magazine head entry (t = 0) in early and late FR1 training. There was a significant effect of time bin, but no effect of training phase or interaction (two-way ANOVA: time bin, $F_{7,27} = 11.44$, $p < 0.0001$; phase, $F_{1,4} = 0.0013$, $p = 0.97$; time bin x phase, $F_{7,28} = 1.21$, $p = 0.33$). (D) Comparison of the AUC from 7.5 to 10s following head entry in early and late FR1 training. There was a trend of greater activity suppression following a rewarded magazine head entry (7.5-10s after entry) in late training compared to early training (paired t test, $p = 0.057$). (Data are represented as mean ± SEM.)

Figure S6. Validation of NAc CRF conditional knock-out

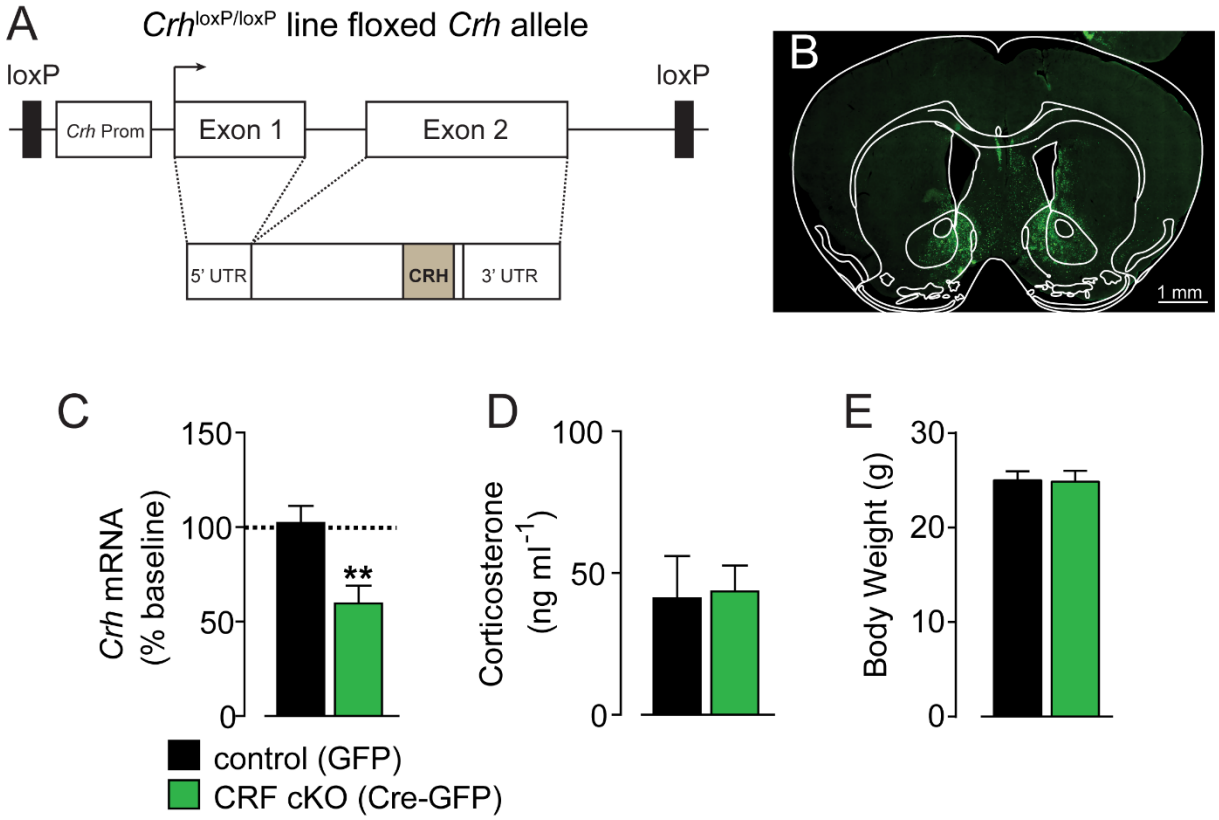

Figure S6, related to Figure 7. Validation of NAc CRF conditional knock-out (A) Schematic of floxed *Crh* locus from the *Crh*$^{loxP/loxP}$ mice used to generate conditional knock-outs. (B) Representative image from *Crh*$^{loxP/loxP}$ mouse injected bilaterally with AAV5-CMV-Cre-GFP (CRF cKO) into NAc. (C) *Crh* mRNA in NAc of control (AAV5-CMV-GFP) or CRF cKO mice after viral injection. RT-qPCR was used to quantify *Crh* mRNA. All values were normalized to average control *Crh*. cKO mice had significantly reduced *Crh* (normalized control: 1.09 ± 09, N = 6; normalized CRF cKO: 0.59 ± 0.09, N = 7, unpaired t-test, p = 0.0084). (D) Corticosterone measured from trunk blood of control and CRF cKO mice. There was no impact of NAc CRF cKO on plasma corticosterone from trunk blood. (E) Body weight of control and CRF cKO mice. There was no difference between groups. (Data are represented as mean ± SEM.) (**p < 0.01)

Figure S7. Additional behavioral data from NAc CRF knock-out experiments

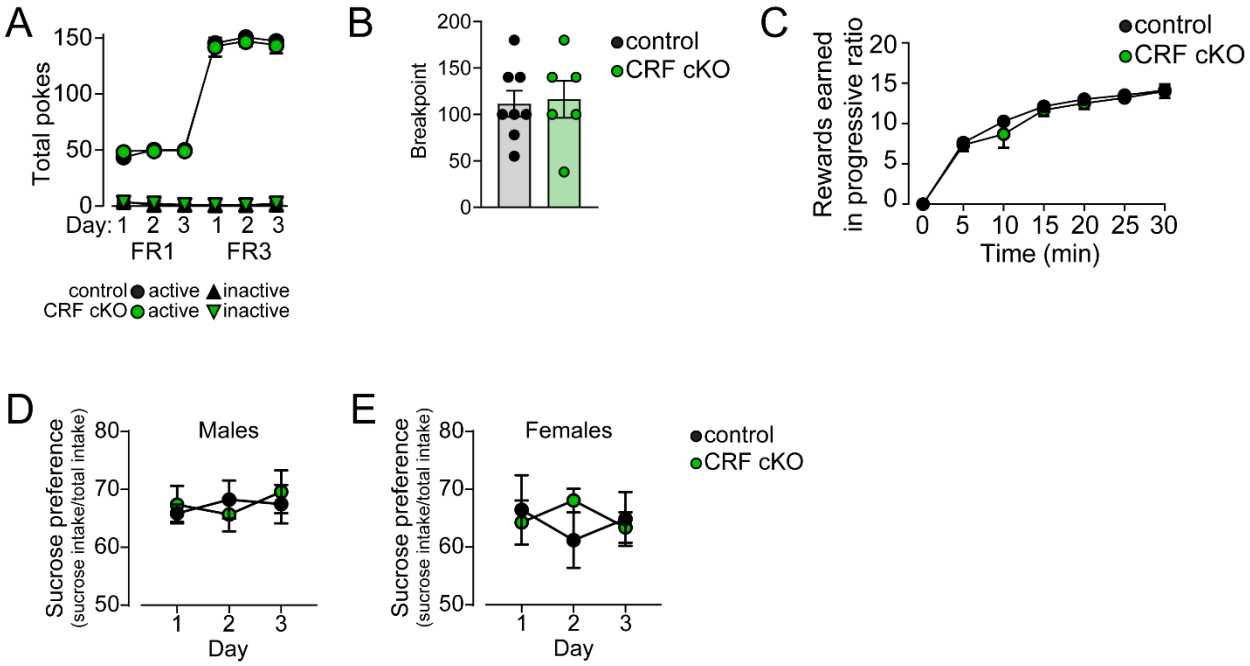

Figure S7, related to Figure 7. Additional behavioral data from NAc CRF knock-out experiments (A) Daily total pokes to active (circles) and inactive (triangles) nose ports from control (black) and CRF cKO (green) mice. There was no difference in total pokes between groups during fixed ratio 1 (FR1) or fixed ratio 3 (FR3) training. (B) Breakpoint values for control and CRF cKO mice from progressive ratio task. There was no difference in breakpoint between groups. (C) Number of rewards earned over time in progressive ratio task. There was no difference between control and CRF cKO mice in rewards earned over time in the progressive ratio task. (D) Sucrose preference across three days of testing in control and CRF cKO males. There was no difference between groups (two-way repeated measures ANOVA; main effect of day: $F_{2,18} = 0.1566$, $p < 0.8562$; group: $F_{1,9} = 0.01758$, $p = 0.8974$; day x group: $F_{2,18} = 0.2506$, $p = 0.7810$). (E) Sucrose preference in control and CRF cKO females. There was no difference between groups (two-way repeated measures ANOVA; main effect of day: $F_{2,16} = 0.0582$, $p = 0.944$; group: $F_{1,8} = 0.0885$, $p = 0.7736$; day x group: $F_{2,16} = 0.9802$, $p = 0.3967$). (Data are represented as mean ± SEM.)